UNIVERSIDADE D
COIMBRA

Maria Inês Mendes Martins

INNOVATIVE DIELECTRIC MATERIALS FOR PASSIVATION OF INTERFACES IN SOLAR CELLS: A MUSR STUDY

VOLUME 1

Dissertação no âmbito do Mestrado Integrado em Engenharia Física, ramo de Instrumentação, orientada pela Professora Doutora Maria Helena Vieira Alberto e pelo Professor Doutor Rui César do Espírito Santo Vilão e apresentada ao Departamento de Física da Faculdade de Ciências e Tecnologia.

Julho de 2020

Acknowledgments

I have to start by acknowledging Prof. Dr. Helena Vieira Alberto and Prof. Dr Rui César Vilão for their availability, guidance and for being a source of science and liveliness.

Furthermore, I thank the investigation group CFisUC and the Department of Physics for the opportunity of participating in the experiments at PSI, in Switzerland, where the experimental work for this thesis was performed, and ISIS, in the United Kingdom. It was truly enriching to be part of the team in both experiments. I would also like to gratefully acknowledge the help and assistance of Dr. Thomas Prokscha from the Low-Energy Muon Laboratory, during the experiment performed at PSI.

To BiF, a colorful group of people I met through Physics, who never let me have a gray day. And to everyone else I met along the way, who came to check on me during isolation.

This work was supported with funds from the Portuguese National Budget through Fundação para a Ciência e Tecnologia/MCTES under project PTDC/FISMAC/29696/2017.

Resumo

Neste trabalho utilizámos a espetroscopia de muão positivo, μSR, para investigar a interface entre Cu(In,Ga)Se_2 - semicondutor utilizado para a absorção em células solares de filmes finos - e uma camada dielétrica de dióxido de silício, SiO_2. Materiais dielétricos, como o dióxido de silício, são promissores para aplicação na passivação de defeitos presentes na interface de CIGS em células solares baseadas em filmes finos. Estudos realizados em CIGS utilizando μSR mostram uma região junto à superfície na qual o sinal do muão é afetado, o que pode dever-se à sensibilidade do muão aos defeitos na superfície, ou à carga na zona de depleção. Para investigar este efeito, são utilizados sistemas onde o sinal da carga presente na interface pode ser controlado. O trabalho experimental foi executado no instrumento *Low-Energy Muons* (LEM), no Paul Scherrer Institute (PSI), na Suíça. As medidas foram realizadas para energias de implantação de muões entre 3 e 22 keV, de modo a controlar a profundidade média de implantação dos muões na amostra. Uma ferramenta de análise de informação em função da profundidade, previamente aplicada a dados de μSR, foi desenvolvida de modo a melhorar o seu desempenho, e a executar ajustes simultâneos aos dados experimentais, tornando a sua utilização mais fácil. A versão melhorada desta ferramenta foi usada para obter um modelo das propriedades da interface em função da profundidade da amostra. Foram obtidas descrições para a variação da fração diamagnética e da relaxação de spin com a profundidade para todas as amostras, confirmando a funcionalidade da ferramenta de análise de informação de profundidade, e fornecendo informação indispensável para este estudo. Os resultados obtidos para a dependência com a profundidade apontam para a ocorrência de *intermixing* junto à interface, dentro da camada de SiO_2. No entanto, não se observou redução da camada de defeitos na superfície de CIGS devido ao efeito de SiO_2. Observaram-se diferenças entre as interfaces com cargas postivas e negativas, provavelmente devido às diferentes condições de deposição ou devido à sensibilidade do muão à carga.

Palavras-chave: Espetroscopia de Muão Positivo, CIGS, Células solares de filmes finos, Defeitos de interface, Dielétricos

Abstract

Muon spin spectroscopy (μSR) has been used to investigate the interface of the solar cell absorber semiconductor copper indium gallium diselenide (CIGS) with a silicon dioxide (SiO_2) dielectric layer. Dielectric materials like SiO_2 have promising applications on the passivation of interface defects in CIGS thin-film solar cells. μSR studies of CIGS show a region where the muon signal is affected. This can be due to a sensitivity of the muon to a defect surface layer or the charge in the space charge region. To investigate this effect, we use systems where the fixed charge at the interface can be controlled. The experimental work was performed at the Low-Energy Muons (LEM) Laboratory at Paul Scherrer Institute (PSI), in Switzerland. The measurements were conducted for muon implantation energies between 3 to 22 keV, thus controlling the average implantation depth of the muons within the sample. An existing depth-resolved analysis tool for muons was further developed in order to improve its performance, allowing simultaneous fits of the experimental data, and becoming more user-friendly. The improved tool was used to acquire a depth dependent model of the interface properties. A description of diamagnetic fraction and spin relaxation depth variation was obtained for all the samples. This asserted the functionality of the depth-resolved analysis tool while providing useful information for this study. The depth dependence results point to the occurrence of intermixing close to the interface, inside the SiO_2 layer. However, no reduction of the CIGS surface defect layer was observed due to the effect of SiO_2. Differences at the positive and negative interfaces were observed, likely due to different deposition conditions or to the muon sensitivity to the charge.

Keywords: Muon Spin Spectroscopy, CIGS, Thin-film solar cells, Interface defects, Dielectrics

List of Figures

List of Tables

Contents

1

Introduction

1.1 Overview of Renewable Energy Sources

The climate crisis we face and the continuing growth of the global population demands that fossil fuel usage is substituted by implementing cleaner energy production alternatives. This will not only contribute to decreasing pollution but also increase public health, and access to electricity, which in some parts of the globe are the lowest-cost power sources.

Reports show [REN19] nonrenewable sources still hold the majority of global electricity production by the end of 2018, but installed renewable power capacity has increased, achieving about 26.2% (fig. 1.1).

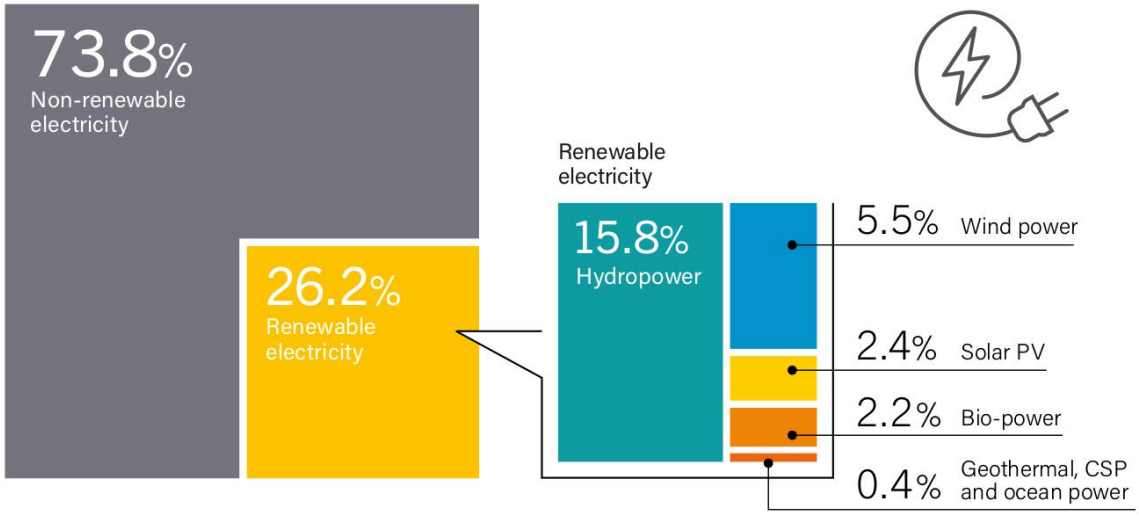

Figure 1.1: Estimated renewable energy share of worldwide electricity production by the end of 2018 (from [REN19]).

In 2018, the solar photovoltaic (PV) accounted for 55% of most recent renewable capacity, with a cumulative global total of 505 GW, which was only 15 GW a decade before (see fig. 1.2). This places solar PV as the fastest-growing energy technology worldwide [REN19],

with China, the United States, Japan, Germany and India being the countries with highest capacity (fig. 1.2).

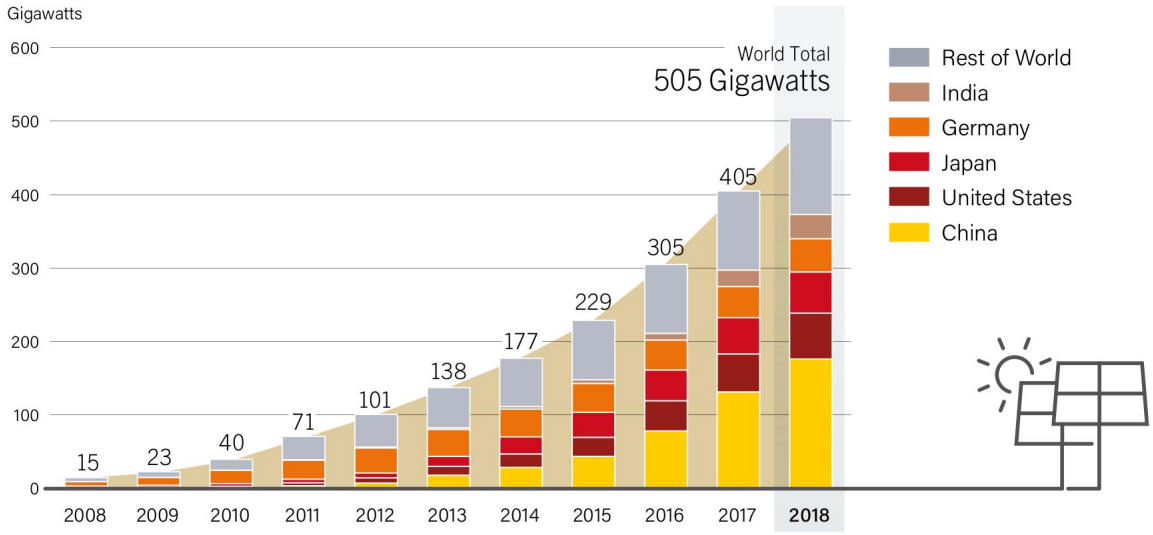

Figure 1.2: Solar photovoltaic capacity, by country and region between 2008 and 2018 (from [REN19]).

1.1.1 Photovoltaic technologies in the market

Photovoltaic technologies use the sunlight reaching the earth to produce electricity. Solar photovoltaic systems are promising given their power conversion efficiency, they are quiet, modular, easy to install and maintain [Son19; ISE15; Pow+17].

To compete with conventional sources, photovoltaic technology needs to be cost efficient and reliable. This translates into two main goals: reducing the material used thus decreasing production cost, and increasing solar energy conversion to electricity. [LE17]

Progress in solar cell efficiency since 1976 can be seen in the chart in fig. 1.3.

First generation solar cells are crystalline silicon (c-Si) based, and can either use polycrystalline (multi-Si) or monocrystalline (mono-Si) Si. It is reported that 93% of solar panels produced use c-Si, followed by second generation photovoltaics relying on thin-film technology, taking up 4.5% of the market [ISE20]. The annual evolution of Si based and thin-films photovoltaic market is presented in fig. 1.4.

c-Si based solar cells are highly competitive, with a power conversion efficiency reaching 26.7% [Gre+19]. However, silicon has an indirect bandgap, consequently, it requires a high thickness absorber. This leads to high production costs, not only because of the quantity of product needed but also due to the fabrication conditions required for Si formation in

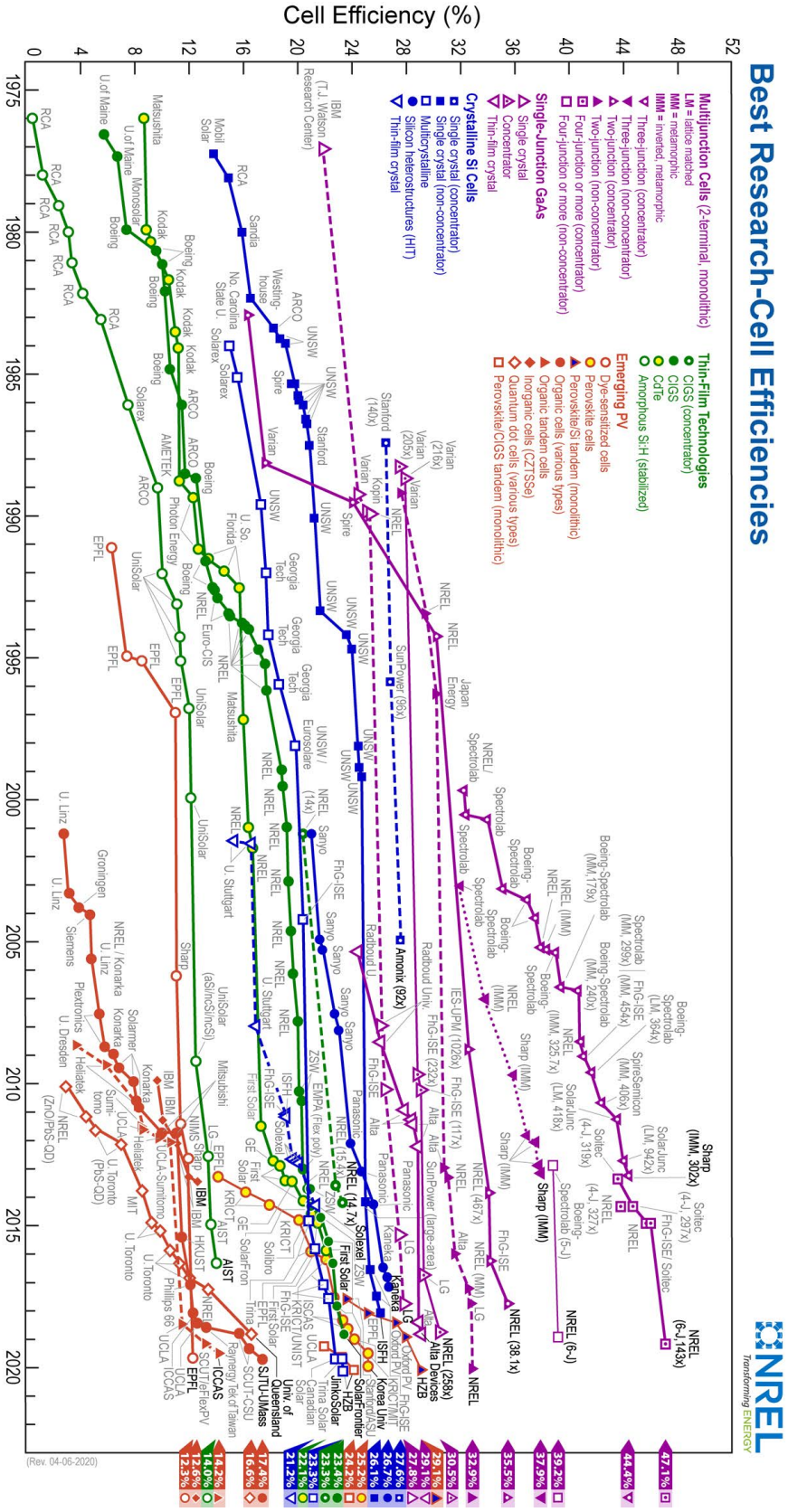

Figure 1.3: Solar cell efficiency evolution by technology since 1976 (from [NRE]).

crystalline form. The payback time for c-Si based system can take up to 2 years, depending on the geographical location, which derives from its high production cost [ISE20].

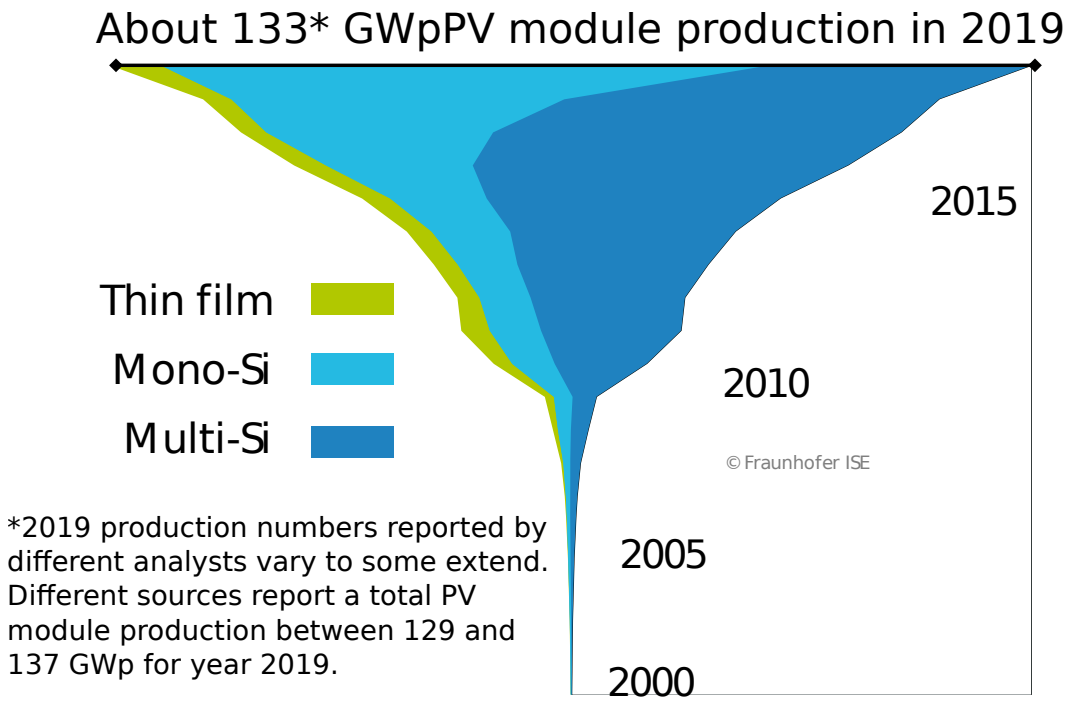

Figure 1.4: Photovoltaic market annual evolution worldwide by technology (from [ISE20]).

Second generation solar cells are also called thin-film solar cells, due to their reduced thickness. The most commercialized thin-film solar cells use cadmium telluride (CdTe), copper indium gallium selenide (CIGS), and amorphous silicon (a-Si). The annual production evolution of these thin-film photovoltaic technologies is presented in fig. 1.5

a-Si based solar cells are the longest-running thin-film photovoltaics in the market, however, they also have the lowest conversion efficiency of 14%. [Gre+19].

CdTe and CIGS technologies are newer, having achieved efficiencies of 22.1% and 23.35% ([LE17; Fro19]), respectively. However, CdTe solar cells contain cadmium which presents health risks for both producer and consumer due to its toxicity. This points CIGS thin-film solar cells as one of the most promising in terms of power conversion. CIGS is a direct bandgap semiconductor with a high absorption coefficient. Their production has a reduced cost because it requires using inexpensive materials, like the glass substrates, it requires less material due to its small thickness, and wastage is reduced [Sie17a]. In comparison to first generation solar cells, the payback time of CIGS based photovoltaic devices is significantly lower, ranging from about 0.78 to under 1 year [Pow+17; ISE20].

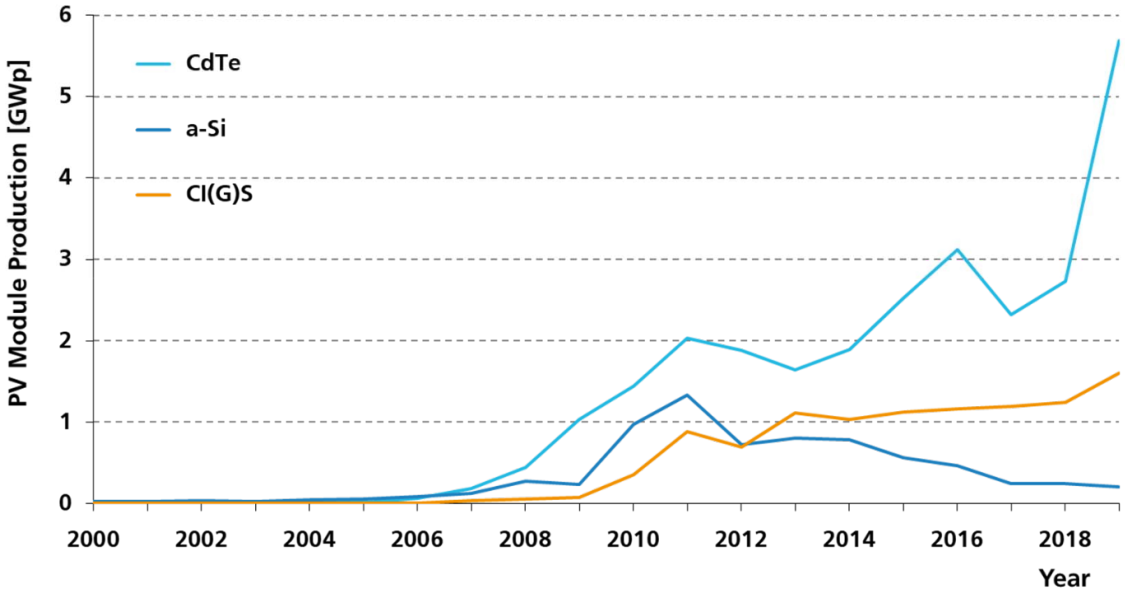

Figure 1.5: Plot of the annual thin-film technologies global production (from [ISE20]).

1.2 Energy Production in Photovoltaic Cells

Photovoltaic devices convert the energy contained in sunlight into electricity based on semiconductor technology. An ideal solar cell has the operation principle of a diode, formed by a semiconductor p-n junction, in parallel with a current source shown in fig. 1.6(b). Therefore the I-V behavior (fig. 1.6(a)) of the junction is described by the ideal diode law

$$I = I_S \left[\exp\left(\frac{eV}{k_B T}\right) - 1 \right] \tag{1.1}$$

where:

- I is the current flowing through the diode
- I_S is the saturation or dark current
- e is the elementary charge
- V is the voltage across the terminals of the diode
- k_B is the Boltzman constant
- T is the temperature.

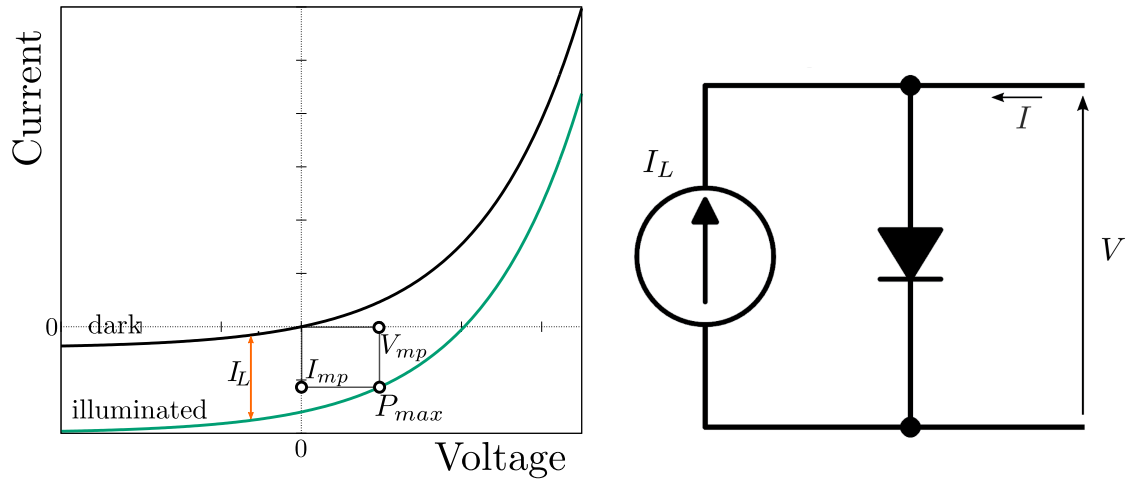

(a) (b)

Figure 1.6: (a) Representation of dark (black) and illuminated (green) I-V characteristic of a photodiode. When the device is illuminated a photocurrent I_L is generated. The area of the biggest rectangle fitted inside the curve is the peak power P_{max}, calculated as the product $I_{mp} \cdot V_{mp}$. **(b)** Equivalent circuit of a solar cell with a current source in parallel with a diode, with a voltage V across the terminals and a current I flowing through the device.

The photovoltaic effect generates a difference in electrical potential in the junction due to exposure to electromagnetic radiation. When the light hits a typical solar cell, its photons are typically absorbed in the space charge region inside the p-type layer, called the absorber. This is the case for thin-film solar cells because the n-type layer is very thin. The electrons will then be excited and become free from their atoms, forming electron-hole pairs particularly abundant in the space charge region. The electric field generated at the junction separates them: the electrons drift to the n-zone and the holes are accelerated to the p-zone (charge carriers flow is represented in fig. 1.7). This process creates a photocurrent from the p to the n layer, I_L, that is proportional to the intensity of incident light, given that each absorbed photon can only produce one e-h pair.
When the cell is illuminated the diode law becomes:

$$I = I_S \left[\exp\left(\frac{eV}{k_B T}\right) - 1 \right] - I_L \tag{1.2}$$

The I-V characteristic of an illuminated solar cell is shown in fig. 1.6(a).

The generated charge carriers are collected using electrical contacts, extracting them to perform work in an outside circuit. However, not all charge carriers generated are converted to electric energy due to several recombination processes [Sme+16].

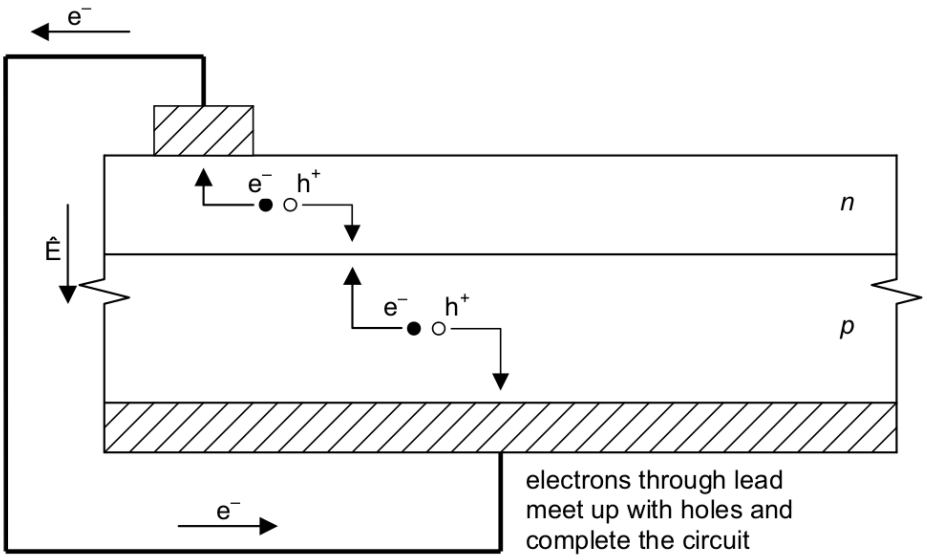

Figure 1.7: Schematic of electrons and holes flow in a p-n junction at short circuit (from [WGW07]).

The parameters that characterize and limit the performance of a solar cell are the short circuit current I_{SC}, the open terminal voltage V_{OC}, the peak power P_{max} and the fill factor FF.

Short circuit current is the maximum current obtained when the voltage is zero (V=0), thus $I_{SC} = -I_L$. This means the current I_{SC} is directly proportional to the illumination

available.

Open terminal voltage is obtained when the current flowing through the cell is zero, $I = 0$. From eq. (1.2), the open circuit voltage is:

$$V_{OC} = \frac{k_B T}{e} \ln\left(\frac{I_L}{I_S} + 1\right) \tag{1.3}$$

At this voltage point, the dark current (I_S) starts to compensate the photocurrent (I_L). The recombination rate has a strong influence on the saturation current, which is higher with increasing recombination, therefore V_{OC} is a measure of recombination taking place in the cell [Sme+16].

Peak power P_{max} is the point in the I-V characteristic in which the solar cell power output is maximum. P_{max} is determined as the product $P_{max} = I_{mp} \cdot V_{mp}$ and graphically it is the biggest rectangle that can be fitted under the I-V curve, shown in fig. 1.6(a), which is when $\frac{d(IV)}{dV} = 0$. The voltage V_{mp} of the peak power can be determined as:

$$V_{mp} = V_{OC} - \frac{kT}{e} \ln\left(\frac{eV_{mp}}{kT} + 1\right) \tag{1.4}$$

Fill Factor is the ratio between the peak power and the product of V_{OC} and I_{SC},

$$FF = \frac{V_{mp} \cdot I_{mp}}{V_{OC} \cdot I_{SC}} \tag{1.5}$$

This parameter is used to assess the quality of the cell junction and to measure its series resistance. Solar cells with fill factor FF closer to unity are considered of higher quality [WGW07].

The final parameter to evaluate the performance is the conversion efficiency of light into electric power of the cell. The efficiency η can be calculated from these parameters as the ratio between the cell power output and the incident solar power

$$\eta = \frac{P_{out}}{P_{in}} = \frac{P_{max}}{P_{in}} = \frac{FF \cdot V_{OC} \cdot I_{SC}}{P_{in}} \tag{1.6}$$

1.3 CIGS based thin-film Solar Cells

CIGS based thin-film devices use $Cu(In,Ga)Se_2$ as the absorber, which will form a p-n junction with the n-type buffer layer, typically made of Cadmium Sulfide (CdS). These cells have reduced thickness compared to first generation solar cells, requiring a substrate for mechanical support. The most efficient cells to date are grown on soda lime glass, but flexible cells can also be obtained by using substrates like polyimide films and stainless steel [Son19]. CIGS is then deposited on top of the Mo back contact. The buffer layer forms a p-n junction with the absorber. Following the buffer layer, there is a bilayer window which transmits the sunlight into the absorber. This bilayer is also called the front contact and is made of intrinsic zinc oxide (IZO) coated with Al-doped ZnO (AZO).

In 2019, the record efficiency of 23.35% for power conversion was achieved with a Cd-free CIGS thin-film solar cell, which uses a $Zn(O,S,OH)_x/Zn_{0.75}Mg_{0.25}$ double buffer layer [Nak+19].

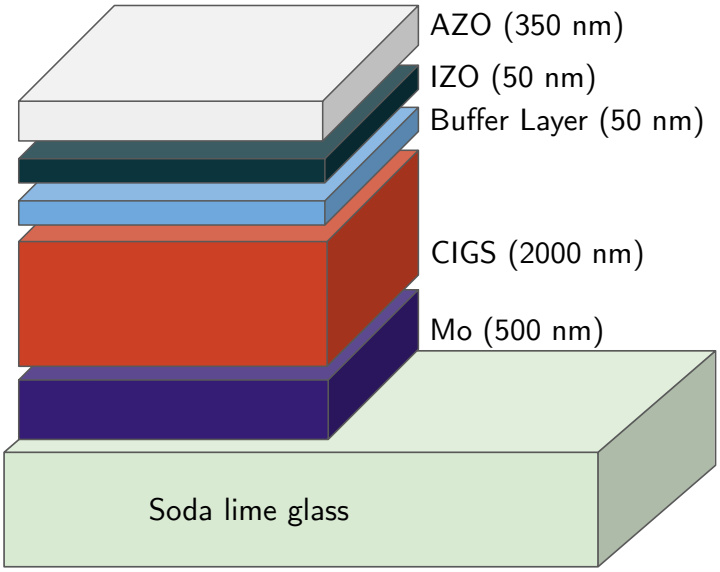

Figure 1.8: CIGS solar cell structure with the approximate thickness of each layer for optimized performance. (Inspired by [Mol16; Bro11])

Figure 1.8 represents the typical structure of a CIGS thin-film solar cell. The main aspects of each layer and its role will be presented in this section.

1.3.1 Soda lime substrate

A soda lime glass substrate is used for mechanical support in the most efficient thin-film CIGS solar cells. The typical composition of soda lime glass is typically about 75% silica

(SiO_2), with the addition of sodium oxide (Na_2O), and calcium oxide (CaO) [KAB17].

This substrate can undergo processing temperatures above 600 °C, offering a very good match to the CIGS and Mo thermal coefficients [Mol16]. During CIGS growth at high temperature, Na diffusion from the substrate is enhanced which improves the device performance [RS17].

1.3.2 Mo back contact

On top of the substrate, there is a molybdenum (Mo) low resistivity contact which transports the photogenerated holes outside the cell. Mo is commonly used due to its relative reduced cost, and high melting point [SS11]. Mo is permeable to alkali elements allowing Na diffusion from the substrate to the CIGS layer, and Na doping plays an important role Cu poor CIGS thin-films [Sie17b]. This layer also has a high reflectance in the visible spectrum, which means some of the light not absorbed initially in the absorber layer is reflected back [Sal11].

The junction CIGS/Mo forms a Schottky barrier but the voltage measured drop across the junction indicates it is an ohmic contact. This effect is observed due to the presence of a MoS_2 layer at the interface which is formed during CIGS deposition at high temperatures [Wad+01].

1.3.3 CIGS absorber layer

CIGS is a I-III-VI_2 semiconductor with a high absorption coefficient (10^5 cm^{-1}), making a reduced thickness of 1-3 μm sufficient to absorb most of the light reaching the cell [Pow+17]. Its bandgap can vary between 1.04 and 1.7 eV, depending on Ga and In composition, being maximum if all In is replaced by Ga [Sme+16]. The voltage V_{OC} is also affected by this, as $V_{OC} \sim \frac{E_g}{2}$, thus increased with Ga incorporation and enhancing the device performance as well [Dul+01]. Best efficiency is reported for E_g between 1.02 and 1.12 eV [RS17; Nak+19].

Typically the absorber layer has a Cu-deficient surface, which increases CIGS conductivity. However, in Cu-poor conditions, there are a large number of antisite defects contributing to recombination. [Sie17a]

The properties of CIGS are affected by the growth conditions and deposition technique used. It is typically grown at temperatures between 450 and 600 °C, and higher temperatures usually lead to better cell efficiency [RS17; Rud+05].

1.3.4 Double buffer layer

The state of the art device uses a double buffer layer to replace CdS. CdS was most commonly used as the n-type semiconductor to form the p-n junction in solar cells due to its passivation effect on the CIGS surface and protection against the damage caused by the ZnO layer. However, the toxicity of Cd compounds is a relevant limiting factor.

The Cd-free double layer is placed on top of CIGS forming the p-n junction with the absorber. The solar cell with $Zn(O,S,OH)_x/Zn_{0.75}Mg_{0.25}$ is the first device with a Cd-free buffer layer able to surpass the performance of the conventional Cd-buffered cells [Nak+19]. It is reported that the first layer of $Zn(O,S,OH)_x$ has a negligible or slightly worse effect on the device performance, compared to when CdS was used. However, adding $Zn_{0.75}Mg_{0.25}$ as the second buffer layer significantly contributes to its improvement.

The double buffer has an energy bandgap E_g=3.6 eV, higher than the 2.4 eV of CdS, which helps to eliminate blue light losses, and thus improving I_{SC}. Another positive factor is the reduction in recombination at the buffer/CIGS interface thus increasing V_{OC}.

1.3.5 Intrinsic ZnO (IZO)

The intrinsic ZnO layer is grown with a high resistivity on top of the buffer layer to prevent an unwanted short circuit between the back and front contacts of the device. The IZO layer is slightly n-type to allow electron conduction through the conduction band. [Bro11; ME09] This layer isolates the buffer and the Al-doped ZnO layers, stopping the Al diffusion into the absorber.

1.3.6 Al-doped ZnO (AZO)

The window and front contact is fabricated using Al-doped ZnO (ZnO:Al). It is called window layer because it is a transparent conductive oxide which lets the light enter the cell into the absorber and it is chosen according to its conductivity to avoid resistivity losses and compatibility with further processing [RS17].

The addition of a MgF_2 coating on the surface of the AZO layer contributes to the reduction of light reflection at the air/ZnO:Al interface [Mol16].

Different production techniques can be used having distinct results in terms of cost, cell efficiency and composition, but they will be not presented here.

1.3.7 Interface charge control with SiO_2

The performance of CIGS based solar cells is closely related to the production processes and conditions [Bos+19], as it influences the opto-electronic properties of CIGS. Most recently, CIGS thin-film solar cells development is focused on improving the CIGS interface, which requires a thorough understanding of its electrical properties [Li+18].

Insulator materials like silicon oxide (SiO_2) are used in Si based solar cells in passivation layers [Ver+12], and using a dielectric layer for surface passivation of CIGS is being introduced [Bos+19]. Passivation reduces the number of defects, therefore reducing recombination and improving the electricity generation efficiency in solar cells.

In [Cun+18], the effect of SiO_x on CIGS surface is studied to be used as a passivation layer in CIGS solar cells. The most relevant results for this work derive from different conditions during the deposition process of SiO_x. The technique used for these samples was plasma enhanced vapor deposition at temperature and frequency conditions: T=300 °C at high frequency, and T=150 °C at high and low frequencies.

The photoluminescence measurements point to the presence of a higher number of recombination channels at CIGS surface when SiO_x is deposited at a temperature T=300 °C, which is attributed to CIGS surface modifications. Furthermore, measures of insulator charge show that for SiO_x, depending on the deposition frequency the polarity of the insulator layer can be inverted: positive for high frequency and negative for low frequency.

The goal of this work is to study the passivation effect on the interface of CIGS and SiO_2. The properties of silicon interfaces, namely with SiO_x have become very well known due to its dominant utilization in semiconductor technologies [FPS08], therefore SiO_x/Si will be used as benchmark. Muon spin spectroscopy is a depth-sensitive technique, which provides a measure of the interface and surface width defect layers, whereas photoluminescence only provides qualitative information.

A depth-resolved analysis tool for muon spin spectroscopy by Simões et al. is also developed during this work in order to perform more complex simultaneous fits of experimental data sets.

2

State of the Art

2.1 Muon: a probe in depth studies

2.1.1 Muon

The muon (μ) is an elementary particle present in nature and one of the main constituent of cosmic rays. As a lepton, it does not interact through strong force and it is comparable to a heavy electron. Like the electron, the muon (μ^-) has negative charge and has a positively charged antiparticle: the positive muon (μ^+).

In condensed matter physics and chemistry the muon is used as an analogue of a proton and as a lighter pseudo-isotope of hydrogen. Throughout this work, we will use the consideration of the pseudo-isotope character of the positive muon, which we will henceforth simply call muon.

As previously stated, the value of its mass is intermediate between the mass of an electron and the proton, as well as the values of magnetic moment. Table 2.1 presents a useful comparison between the muon, electron and proton properties.

	charge	spin	mass	moment
e	$\pm e$	$\frac{1}{2}$	m_e	$657\mu_p$
μ			$207m_e$	$3.18\mu_p$
p			$1836m_e$	μ_p

Table 2.1: Charge, spin, mass and magnetic moment of the electron, muon and proton. The mass and magnetic moment of each particle are presented in terms of the electron mass (m_e) and the proton magnetic moment (μ_p), respectively. (Adapted from [Blu99].)

Table 2.2 contains the most relevant properties of the muon for Muon Spin Spectroscopy (μSR). These properties are lifetime, charge, magnetic moment and gyromagnetic ratio. The gyromagnetic ratio is the proportionality constant between angular momentum and magnetic momentum.

Lifetime	$\tau_\mu = 2.1969811(22)\ \mu s$
Charge	$+e$
Mass	$105.6583745(24)\ \mathrm{MeV}/c^2$
Magnetic Moment	$m_\mu = 4.836 \times 10^{-3} \mu_B$
Gyromagnetic ratio	$\gamma_\mu = 2\pi \times 135.538817\ \mathrm{MHz/T}$

Table 2.2: Main Properties of the muon. The magnetic moment is given in terms of the Bohr magneton ($\mu_B = 9.274 \times 10^{-24}$ J/T) .(Adapted from [Ama19]).

In the presence of a transverse magnetic field **B**, the muon spin precesses at the Larmor frequency (fig. 2.1):

$$\omega_L = \gamma_\mu B \tag{2.1}$$

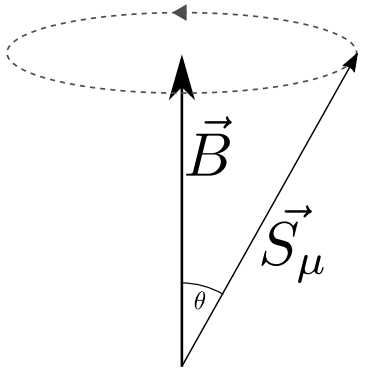

Figure 2.1: Representation of muon spin precession with an applied field **B** at angle θ.

The muon is an unstable particle and its decay is a three-body process with the emission of a positron (e^+):

$$\mu^+ \rightarrow e^+ + \nu_e + \bar{\nu}_\mu \tag{2.2}$$

This emission results in an anisotropic positron energy distribution dependent on the orientation of the muon spin. The positron is preferentially emitted in the direction of the muon spin at the time of decay, as represented in fig. 2.2. The normalized positron energy over the maximum emission energy is $\epsilon = \frac{E_{e+}}{E_{max}}$.

2.1.2 Muon Production

"Man-made" muons are obtained using high energy proton beams. The protons are first accelerated and then fired into a target, usually made of graphite. The outcome of this

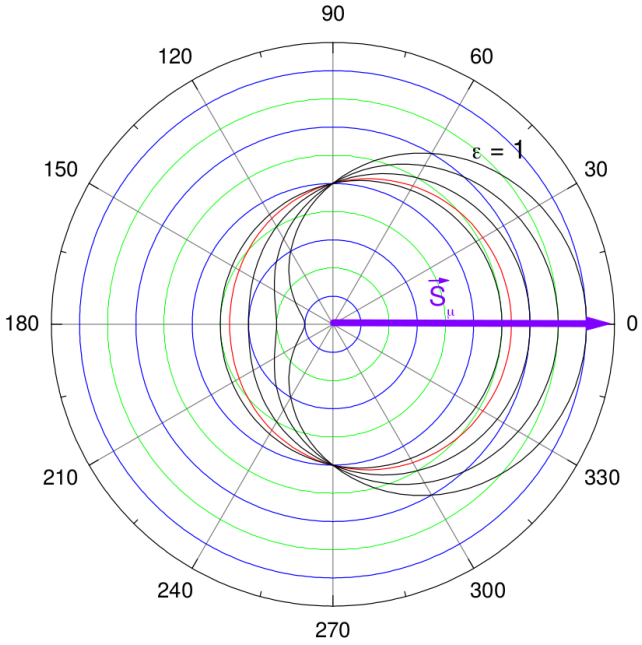

Figure 2.2: Spatial distribution of emitted positrons with relation to the muon spin orientation at decay (0°). The case where the normalized energy is maximum $\epsilon = 1$ is represented.The red line represents the average over all positron energies (from [Vil07])

.

process is the production of a pion (π^+), as follows:

$$p + p \rightarrow \pi^+ + p + n \tag{2.3}$$

The positive pion is an unstable particle with a mean lifetime of 26 ns and zero spin. Its primary decay mode is into a muon and a muon-neutrino (fig. 2.3):

$$\pi^+ \rightarrow \mu^+ + \nu_\mu \tag{2.4}$$

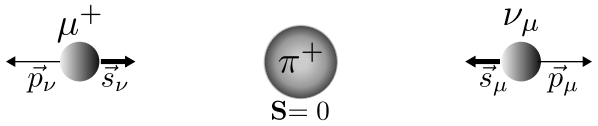

Figure 2.3: Schematic representation of the positive pion (π^+) decay into a positive muon (μ^+) and a muon-neutrino (ν_μ).

The conservation of linear momentum and energy has interesting implications for this decay. The two body decay creates a muon and a muon-neutrino with opposite and equal momentum, in the rest frame of the pion. The neutrino has negative helicity, which means its spin is aligned antiparallel with its momentum. As the pion has zero spin the muon will too have its spin with opposite direction to the momentum.

Considering this, it is possible to obtain a beam of completely spin-polarized muons. If only pions at rest are selected, the muons produced flying in a given direction will have their spins aligned antiparallel to their momentum.

The muons produced have a kinetic energy of 4.1 MeV [BM04].

2.1.3 The μSR Technique

In Muon Spin Spectroscopy (μSR) muons are implanted into a sample and stay there until they decay.

The muon spin is a highly sensitive microscopic probe. It is mainly a probe of local magnetic fields, but through muonium formation and charge exchange with the solid it can interact with local charges as well. This makes it a possible probe for defect-rich and charged regions, providing useful information about the physical properties of the materials they are implanted into.

The detector system needs to have positron detectors but also a first muon detector to obtain the arrival time of the muon.

The incoming muon is first detected by the scintillator, and it starts the time counter, which is stopped when a positron is detected.

The positron detection apparatus, represented in fig. 2.4, is divided, as it requires a minimum of two detectors: backward (B) and forward (F), located upstream and downstream of the sample, respectively.

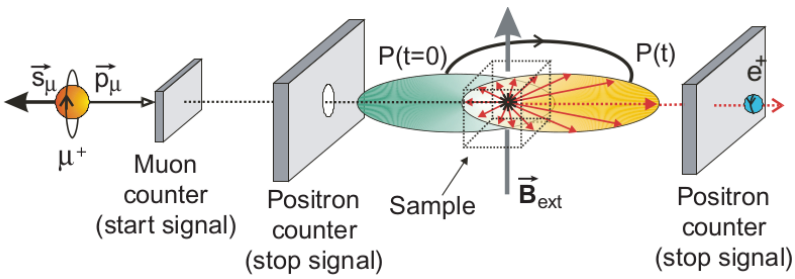

Figure 2.4: Representation of the experimental setup in an applied transverse field. (from [BM04].)

The measurements using the μSR technique can be performed applying a longitudinal (LF) or transverse (TF) magnetic field, or at zero-field (ZF), depending on the study to be done. In LF experiments an external magnetic field parallel to the muon spin direction is applied in order to study the time evolution of the muon spin relaxation. When an external field is applied perpendicular to the muon spin (TF geometry) the μSR signal obtained will be the spin rotation as a function of time.

As mentioned previously, the muon has an average lifetime τ_μ=2.19 μs and decays after a time t with a probability proportional to $exp\left(\frac{t}{\tau_\mu}\right)$ [Blu99]. Detection of the decay positron gives useful information about the direction of the muon spin at the time of decay. Therefore, it is possible to reconstruct the time evolution of the muon spin inside the sample. Due to the preferential emission in the direction of the muon spin, there is an asymmetry in detection of positrons. This asymmetry can be simply estimated as the normalized difference of positrons detected in the upstream F and the downstream B detectors (eq. (2.5).

$$A = \frac{N_B - N_F}{N_B + B_F} \tag{2.5}$$

where N_B and N_F are the number of positrons detected on the backward and forward detectors, respectively and $N_B + N_F$ is the total number of events detected.

There can be two types of muon beams, continuous wave (CW) and pulsed beams, distinguished by their time structures.

In a CW beam only one muon at a time is in the sample, arriving intermittently. Each muon is detected in the setup to start the clock, which stops after the positron is detected. Some problems may arise if a second muon arrives at the sample before the first one has decayed. In this case, two positrons are detected without being possible to identify which muon decay each positron resulted from. Therefore, this event is discarded. The occurrence of these pile-up events is usually prevented by reducing the arrival frequency of the muons. CW sources can provide a very high time resolution, but usually present a relatively large background, which limits the measurements of slow signals.

For pulsed beams a group of muons arrives at the sample, without individual detection of the muons. Each decay positron will be detected and timed according to the moment of the beam arrival. This setup does not require a muon counter. However, it needs a very high number of positron detectors due to the simultaneous arrival of a large number of muons. In pulsed sources the background events are therefore much reduced due to the simultaneous arrival of a large number of muons. However, the arrival time of the muons has a distribution with width τ_w (fig. 2.5), which sets an upper limit to the observable frequencies.

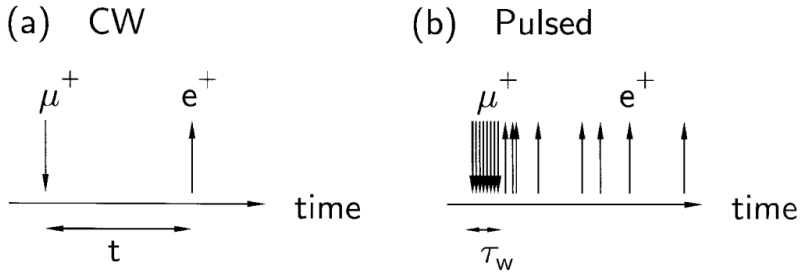

Figure 2.5: Schematic illustration of the two types of muon beam (a) continuous wave and (b) pulsed. (from [Blu99].)

2.1.4 Low Energy Muons

As mentioned before, the kinetic energy of the muons produced in the beamline from the pions stopped at the of the beamline target is 4.1 MeV. These are called surface muons and stop at a depth between 0.1 mm and 1 mm in solids. Surface muons are therefore unable to provide any useful information for the study of thin-films with widths in the range of tens to hundreds of nanometers. Through energy moderation techniques, it is possible to obtain slow muons with energies below 100 keV and a stopping range from fractions of a nanometer to hundreds of nanometers [BM04].

The reduction of the kinetic energy of surface muons is achieved through moderation. Moderation can be done using a thin layer of a solid material with a low reactivity: the moderator. The moderator is typically a condensed Van der Waals gas, used to obtain a beam of low-energy muons with a well defined energy spectrum. The following steps summarize the process occurring when the muon beam is fired into a foil layer, having a thickness of 100 nm, on the back of the thin moderator layer:

1. The surface muons reach a thin foil substrate where they start losing energy by Coulomb collisions with the electrons, excitation and ionization of the atoms.

2. When the muons energy is around 10 keV, and the kinetic energy is almost completely lost, muonium formation cycles start. In this process, the muon will capture an electron creating a muonium atom, losing it sometime after during collisions.

3. The cryosolids, such as krypton, argon, nitrogen used in the moderator layer, have relatively high band-gap energies (between 11 and 22 eV) [Ama19]. When the muons reach an energy of the order of the band-gap, the energy loss processes cease. At these low energies, the muons are left unperturbed and are ejected.

At the end of this procedure, a beam of very slow or epithermal muons (with energies of the order of 15 eV) are obtained. These muons conserve their initial polarization, as the energy loss due to electron Coulomb scattering is very fast and does not affect it significantly. This is the moderation method used in the Low-Energy Muon (LEM) Laboratory at the Paul Scherrer Institute in Switzerland, the single slow-muon facility, where measurements for this work were performed. Presently the rate of muons arriving at the moderator surface is 2×10^8 μ^+/s. The epithermal muons are finally accelerated with a positive potential between 12 and 20 kV to energies in the range of 1 to 30 keV. The muons arrival rate at the sample is currently 4.5×10^3 μ^+/s.

A schematic representation of the experimental setup of the Low-Energy Muon (LEM) experiment beamline is presented in fig. 2.6.

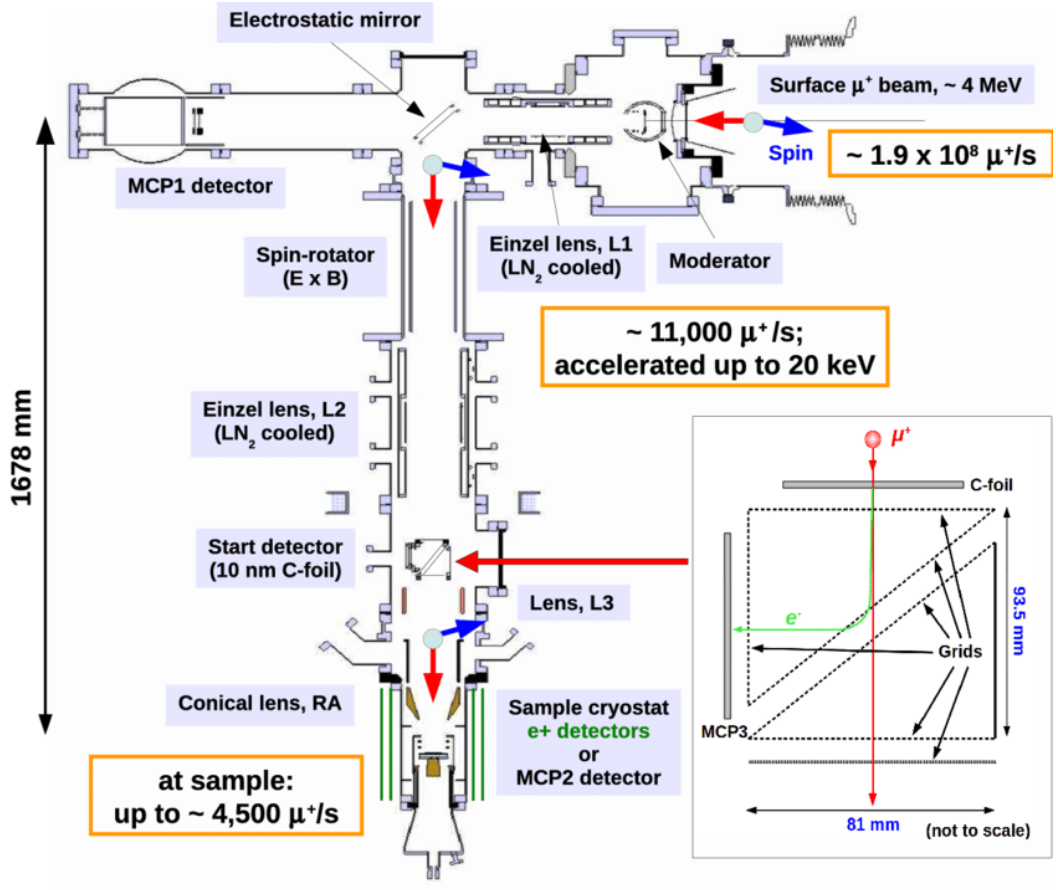

Figure 2.6: Schematic of te Low-Energy Muon Laboratory beamline. The 4 MeV surface μ^+ beam is moderated to an energy of about 15 eV. These epithermal muons are accelerated to with a positive potential to obtain muons with energies up to 20 keV. The low-energy muons can then be implanted into the sample with energies in the range 0.5 to 30 keV (from [Gro].)

2.1.5 Muonium Formation

When implated into a sample, the muon can capture an electron forming an atom like muonium state, Mu ($\mu^+ + e^-$). This state can be seen as a light pseudo-isotope of hydrogen given its analogue electronic properties. In muonium the coupling of the muon ($\mathbf{S}_\mu$) and the electron ($\mathbf{S}_e$) spins is described by the hyperfine interaction Hamiltonian:

$$\mathcal{H} = hA\mathbf{S}_\mu \cdot \mathbf{S}_e \tag{2.6}$$

where $A = 4.463302765(53)$ GHz is the hyperfine interaction value in vacuum [Liu+99]. $\mathbf{S}_\mu$ and $\mathbf{S}_e$ are the spin operators of the muon and electron, respectively.

In the presence of a magnetic field, the Hamiltonian from eq. (2.6) has the addition of the

Zeeman effect between applied magnetic field and the muon and electron spins:

$$\mathcal{H} = hA\mathbf{S}_\mu \cdot \mathbf{S}_e - \mathcal{M}_\mu \cdot \mathbf{B} - \mathcal{M}_e \cdot \mathbf{B} \tag{2.7}$$

with $\mathcal{M}_\mu$ and $\mathcal{M}_e$ the magnetic moment operators of the muon and electron, respectively.

Transverse-field μSR allows for the observation of simultaneous occurring muonium states. The spectra in fig. 2.7 were obtained for quartz and silicon samples, measured in an applied transverse magnetic field B =10 mT [Pat88].

The frequency peak at around 1.36 MHz is present in both spectra and corresponds to the Larmor precession component. The two frequencies centered around 139 MHz correspond to the typical muonium frequencies [Pat88]. In the silicon spectra is, however, observed another peak centered at around 39 MHz, which was considered an "anomalous" state at the time of the discovery. This "anomalous" muonium was later assigned to a neutral state (μ^+e^-), which has a much smaller hyperfine interaction [CS86; Kie+88].

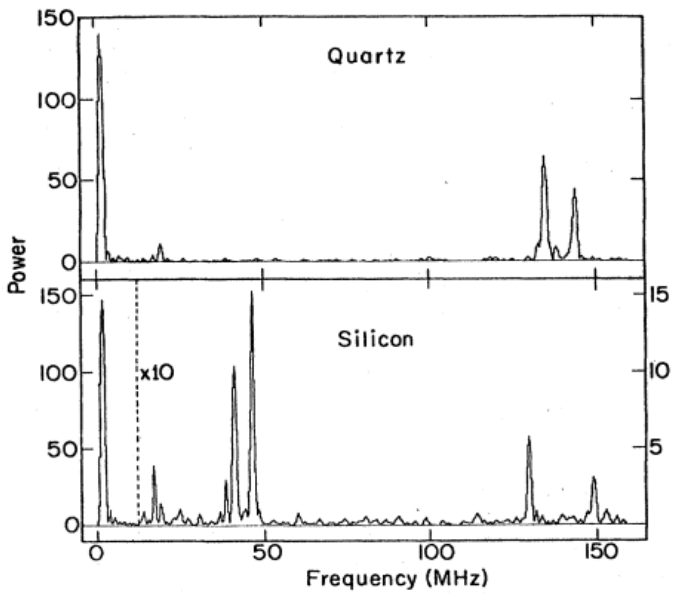

Figure 2.7: Frequency μSR spectra for quartz at room temperature and for a *p-type* silicon sample at T =77 K with an applied transverse field $\mathbf{B}$ = 10 mT. (from [Bre+73].)

The observation of the spectra in fig. 2.7 gives information about the existence of three different Mu states in silicon at 77 K [Bre+73; Pat88].

- Atom-like muonium, Mu^0_{atom}, is a neutral (paramagnetic) configuration formed when a muon captures an electron, having a strong hyperfine interaction in the order of the GHz or the vacuum value.

- Bound muonium, Mu^0_{bound}, is a neutral (paramagnetic) configuration resulting from a distorted electronic cloud around the muon. This state has a much lower and anisotropic hyperfine interaction, and is associated to the "anomalous" muonium.
- Positive muonium, Mu^+, is a diamagnetic configuration usually associated to the final ionized state of the bound state.

There is another muonium configuration predicted theoretically, which is negative muonium (Mu^-). Mu^- is a diamagnetic state, associated to the double capture of an electron [Kua+89]. Since it is produced in a two-stepped process, its formation has a very low probability, and it is possible to admit the diamagnetic signal observed does not have a contribution due to the formation of this latter state [Alb+18].

As previously stated the atom-like muonium can be distinguished from the diamagnetic states due to its strong hyperfine coupling with the electron. This leads to a spin precession frequency about 103 times greater for Mu^0_{atom} [Ama19]. The μSR signal obtained is the asymmetry, which is determined by the amplitude of the precession. The asymmetry of the diamagnetic and paramagnetic species is proportional to the fraction of muons in those particular states.

It has been reported that muons in chalcopyrites, such as CIGS, thermalize mainly in a diamagnetic fraction [Vil+03b]. The asymmetry time evolution for a CIGS sample measured at T=50 K in a transverse field B=10 mT at the Low-Energy Muon Laboratory (LEM) is represented in fig. 2.8. This muon signal can be described by a Gaussian-damped cosine at the Larmor frequency ω [Vil+03a; Alb+18]:

$$A(t) = A_{dia}\, \mathrm{e}^{-\frac{1}{2}\sigma^2 t^2} \cos\left(\omega t + \phi\right) \tag{2.8}$$

where A_{dia} is the signal amplitude, σ is the Gaussian relaxation rate, and ϕ is the phase. The relaxation rate is related to the loss of polarization of the muon spin ensemble due to magnetic interactions.

For CIGS, a fraction of the muon signal is missing. Missing fraction is observed when muons strongly interact inside the sample, during its implantation phase, completely losing their polarization, and cannot be identified with spectroscopy [Vil07].

Experimentally, a sample of silver (Ag) is used to obtain the maximum experimental value of asymmetry, for a given geometry and set of detectors, and it is usually around $A_{max} \sim 0.25$ [Blu99]. The asymmetry A_{dia} is used to calculate the corresponding diamagnetic fraction f_{dia}:

$$f_{dia} = \frac{A_{dia}}{A_{max}} \tag{2.9}$$

as the ratio between A_{dia} and the maximum asymmetry A_{max}.

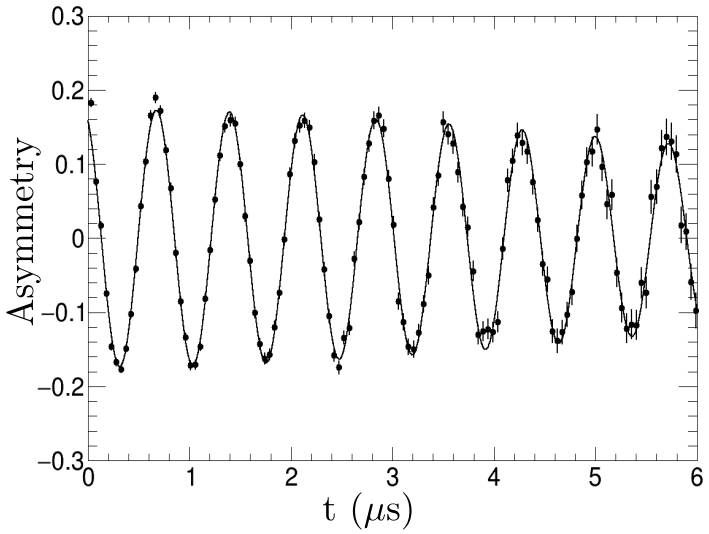

Figure 2.8: Asymmetry signal for a CIGS sample at T=50 K in transverse field B=10 mT measured at the Low-Energy Muon (LEM) Laboratory. The line is fitted to a Gaussian-damped cosine assigned to the bound and positive muonium.

2.2 μSR in the study of CIGS

μSR has been applied successfully in the study of the surface and interface of semiconductors [Alb+18]. By implanting slow muons in these samples, as described in section 2.1, it is possible to obtain depth-resolved information in the order of 10 to 100 nm. The muon stopping depth is related to the implantation energy, therefore, by changing it, in the range of 1 to 30 keV, one can use the muon as a probe for specific regions of the material.

In the case of films with p-type Cu(In,Ga)Se_2 (CIGS), several studies have been performed to understand its surface and the interface created when other materials are placed on top of it, such as n-type CdS and ZnSnO [Alb+18], forming a p-n junction for solar-cell devices.

2.2.1 Previous experiments

Cadmium sulfide (CdS) is currently the most commonly used n-type material in solar cells using CIGS as absorber. CdS has an important role in reconstructing the CIGS defect-rich surface, but the use of cadmium in the buffer layer may represent an environmental hazard. The elements present in CIGS, indium (In) and gallium (Ga), are not abundant on earth, and so the possibility to use other substances as solar cell absorbers has been under scrutiny. CZTS is a potential CIGS substitute, as it has a similar structure but is composed of earth-abundant elements.

In [Alb+18] , the μSR technique was used to compare the effect of CdS in two different absorbers, CIGS and CZTS. The effect of two distinct buffer layers on CIGS was also studied, comparing CdS/CIGS and ZnSnO/CIGS. The advantage of ZnSnO is that it is a Cd-free material, thus having a reduced toxicity.

Most of the measurements were performed at an external transverse magnetic field B=10 mT and at temperature 5, 40 or 50 K. The muons were implanted with variable energy from 2 to 25 keV.

Experimentally, the measured μSR parameters are obtained as a function of the muon implantation energy. To have a correlation between the implantation energy and the muon stopping depth, a Monte Carlo simulation TRIM.SP was performed for every sample, as exemplified in fig. 2.9(a). This simulation calculates the probability per unit length that a muon implanted with energy E stops at depth x, P(x,E). The relative fractions w_p and w_n of muons stopping on the p-type (absorber) and n-type (buffer) layers, respectively, are also obtained fig. 2.9(b).

Based on the values w_p and w_n, it is possible to calculate the predicted value of the diamag-

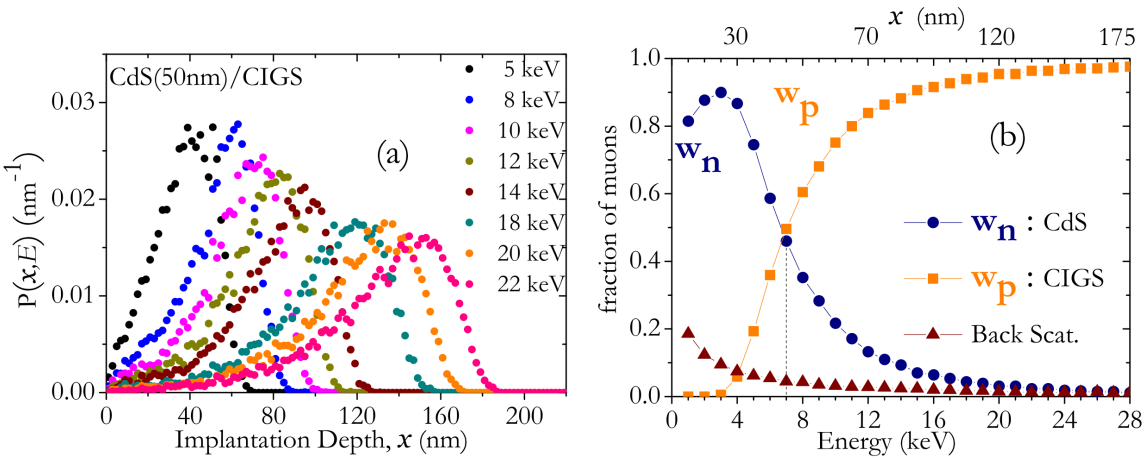

Figure 2.9: (a) muon stopping probability per unit length for different implantation energies as a function of stopping depth. (b) Representation of the muons stopping fraction in each material, as a function of implantation energy and depth x. (from [Alb+18])

netic fraction, with the following weighted average:

$$f_{dia}^{pred}(x) = w_n(x) f_{dia}^{n} + w_p(x) f_{dia}^{p} \tag{2.10}$$

where f_{dia}^{n} and f_{dia}^{p} are the typical diamagnetic fractions for each n-type and p-type material, respectively.

In [Alb+18] the effect was analyzed by calculating the difference, Δf, between the experimental values f_{dia} and the predicted values f_{dia}^{pred}:

$$\Delta f = f_{dia} - f_{dia}^{pred} \tag{2.11}$$

Δf is expected to be zero if the experimental value for the diamagnetic fraction arises simply from the distribution of the muons in the different (assumed non-interacting) layers.

The diamagnetic fraction f_{dia} was obtained for the samples measured at T=50K. The experimental results for the variation Δf are represented in fig. 2.10(a). Δf is found to be negative for the heterostructures in the interface region and in the bulk samples at the film surface, meaning the diamagnetic fraction is reduced with respect to the purely geometrical distribution. For the analysis of the μSR data obtained, it is possible to model of the drop in the diamagnetic fraction as a square well function $Y(x)$:

$$Y(x) = -C \text{ for } a < x < b, \tag{2.12}$$

which means Y=0, except between the implantation depths a and b, where the depth from the pure average (eq. (2.10)) is larger, here modeled by a dip with depth C. The implantation

probability at a certain region, between a and b is given by the numerical integration of $P(x,E)$, the muon stopping probability per unit length:

$$P(a,b,E) = \int_a^b P(x,E)dx \tag{2.13}$$

Therefore, the function Δf as a function of implantation energy, $\Delta f(E)$, becomes:

$$\Delta f = -C\ P(a,b,E) \text{ for } a < x < b \tag{2.14}$$

leading to a good description of the experimental data obtained, as plotted in fig. 2.10.

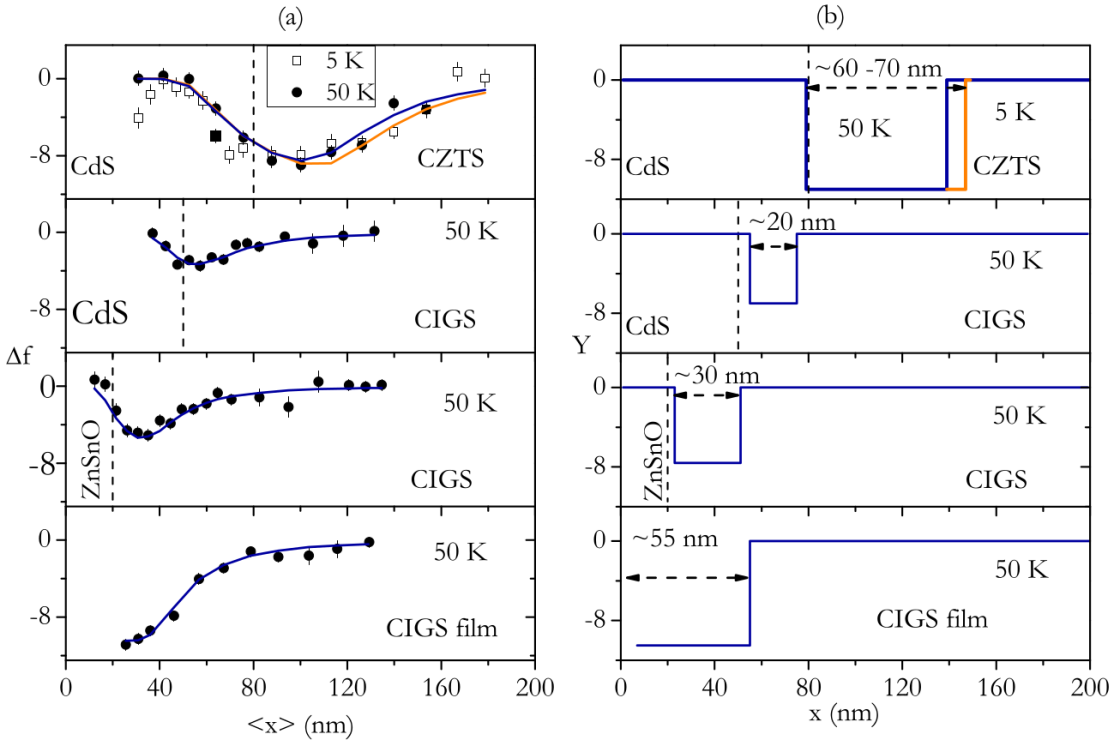

Figure 2.10: (a) Plot of the diamagnetic fraction variation Δf as a function of average implantation depth $\langle x \rangle$. The dotted line represents the interface depth. (b) Square well function $Y(x)$ fitted to the variation Δf as a function of implantation depth. (from [Alb+18])

The main observation of this study was this dip in the diamagnetic fraction at the interface of the p-n junction and at the surface in bulk CIGS and CZTS samples. Two models are discussed in [Alb+18] to explain this effect, both related to the atom like muonium Mu^{0*}_{atom}. We briefly summarize these two models, based on the existence of either charges or defects in the affected region.

Space Charge Region Model (SCR): The muons are seen as being sensitive to the region charge, and it is expected the effect on the fraction is constant, as observed. In this model the variation in the missing and diamagnetic fractions depends if the interstitial muonium stays neutral:

$$Mu^{0*}_{atom} \rightarrow Mu^{0}_{atom} \tag{2.15}$$

or if it captures a hole:

$$Mu^{0*}_{atom} + h^{+} \rightarrow Mu^{+}_{atom} \tag{2.16}$$

The first process contributes to the missing signal, and the formation of positive muonium in eq. (2.16) is related to the diamagnetic fraction. According to this model, the decrease in the diamagnetic fraction is dependent of the concentration of holes in the SCR. The absorber SCR is characterized by a depletion of holes and the process in eq. (2.16) is suppressed, and the diamagnetic fraction presents a dip. The expected values for the SCR are considerably larger than the width measured for the dip region, therefore it is not likely the observed effect is due to the SCR.

Surface Defect Layer Model (SDL): According to this model the muon is sensitive to the presence of defects and unordered regions like the SDL. In this model, two competing mechanisms are proposed:

$$Mu^{0*}_{atom} \rightarrow Mu^{0}_{atom} \tag{2.17}$$

$$Mu^{0*}_{atom} \rightarrow Mu^{0/+}_{bound} \tag{2.18}$$

where $Mu^{0/+}_{bound}$ represents an anion-bound muonium state, which can either be neutral or positive. As mentioned for the SCR model, the process on eq. (2.17) is connected to the missing fraction, while the occurrence of the second mechanism contributes to the diamagnetic fraction. The latter reaction might be inhibited in a surface such as the SDL. The defects present will increase the energy barrier to activate the conversion of eq. (2.18) and thus a decrease in the diamagnetic fraction is observed. The values obtained in this study for Δf dip width are consistent with the SDL width. This means that μSR offers a way to measure the SDL in both films and heterostructures.

The previous analysis demonstrated a square well function was an appropriate fit for the μSR data considering the resolution this technique provides. However, the fitting values were determined manually and the method was limited to only one μSR parameter, the diamagnetic fraction.

2.2.2 The Depth Resolved Analysis Tool

In [Sim+20] a new method was presented to infer a depth dependence from the experimental dependence in energy. The new method is not limited to the analysis of the diamagnetic fraction, as before. It is a simpler approach and can be applied to any μSR parameter. The relation between a given μSR parameter and the implantation depth is calculated based on the stopping probability $P(x,E)$ usually obtained by Monte Carlo Simulation with the code TRIM.SP. This method consists of dividing the sample in layers, assuming a step function is a suitable approximation for the variation of the parameters within the structure. Figure 2.11 is presented as an example of a typical nanostructure, where a thin Al_2O_3 layer is deposited on top of a thin-film of CIGS.

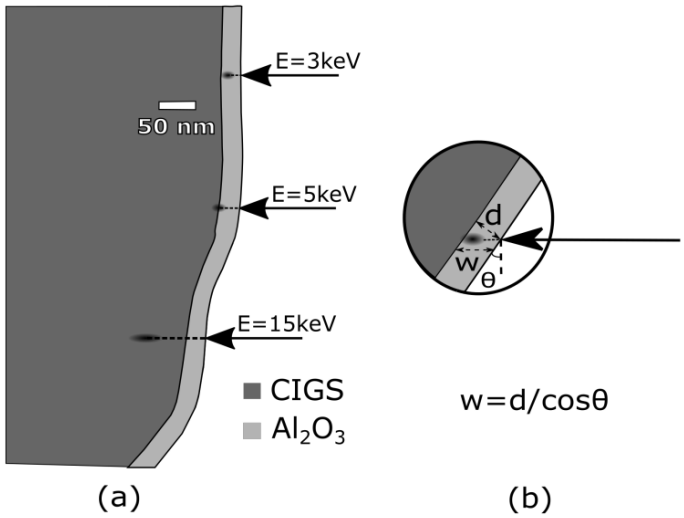

Figure 2.11: (a) Schematic representation of the muon depth implantation for different implantation energies for the Al_2O_3/CIGS heterostructure. Based on a Transmission Electron Microscopy picture. (b) Detail showing the effect of rough surfaces on the exposed layer. The nominal thickness d might different from thickness seen by the probe w, depending on the inclination of the film surface θ. (from [Sim19])

The software named Depth Resolved Analysis for muons (DREAM) implements the method and is exemplified below in the analysis of a semiconductor film of CIGS covered with an aluminum oxide (Al_2O_3) layer. This sample was measured using Low-Energy Muons in order to study the passivation effect of the dielectric oxide Al_2O_3 on the CIGS surface [Sim+20]. The measured value for the thickness of the Al_2O_3 layer by Transmission Electron Microscopy (TEM) was 22(4) nm.

The μSR measurements were performed with the application of a magnetic field B=10mT in transverse field geometry, at a temperature T=40 K and with implantation energy in the range 3-15 keV.

The diamagnetic signal was fitted to an exponentially damped cosine at an angular frequency

close to the Larmor frequency:

$$A(t) = A_{dia} e^{-\lambda t} \cos(\omega t + \phi) \tag{2.19}$$

where A_{dia} is the signal amplitude, λ is the Lorentzian depolarization rate a, ω is the angular frequency and ϕ is the phase. λ, ω, ϕ and f_{dia} are the μSR parameters and are obtained directly as a function of the implantation energy E.

As previously stated, it is reasonable to consider a step function to accurately describe the behavior of the parameters inside the sample. To divide it in layers, it is assumed the μSR parameter has a constant value within the layer and that, given the technique resolution, an abrupt change in this value is expected at the junction interface. Therefore, assuming a heterostructure with three regions :

$$f(x) = \begin{cases} f_{0a} \text{ for } 0 \leq x < a, \\ f_{ab} \text{ for } a \leq x \leq b, \\ f_{b\infty} \text{ for } x > b \end{cases} \tag{2.20}$$

where f_{0a}, f_{ab} and $f_{b\infty}$ are the values of a given parameter f for the regions contained in the ranges $0 \leq x < a$, $a \leq x \leq b$ and $x > b$, respectively. Here, a possible intermediate layer in the region [a,b] is used to describe the passivated CIGS region close to the Al_2O_3 interface. For this model, the parameter f as a function of the implantation energy E, $f(E)$ is calculated as:

$$f(E) = p_{0a}(E) f_{0a} + p_{ab}(E) f_{ab} + p_{b\infty}(E) f_{b\infty} \tag{2.21}$$

where p_{0a}, p_{ab} and $p_{b\infty}$ are the probability the muon stops in the respective depth ranges. The probability p_{ab} is again calculated as seen in eq. (2.13), and a and b are the adjustable parameters determined in order to obtain a proper fit between $f(E)$ and the experimental data.

As a refinement, the authors in [Sim+20] also presents the possibility to allow for a smooth transition between the values of f. This method requires additional parameters and assumes a sigmoidal transition between f_{ab} and $f_{b\infty}$. Therefore, the adaptation of eq. (2.20) and eq. (2.21) is as follows:

$$f(x) = \begin{cases} f_{0a} \text{ for } 0 \leq x < a, \\ f_{ab} \text{ for } a \leq x \leq b, \\ f_{c\infty} + \frac{f_{ab} - f_{c\infty}}{1 + exp\left(\frac{x - x_0}{d}\right)} \\ f_{c\infty} \text{ for } x > c \end{cases} \tag{2.22}$$

where $x_0 = (b + c)/2$ is the center of the smooth transition and d determines its slope. The sigmoidal shape requires that $s << (b + c)/2$, therefore d was defined as $d = (c - b)/10$.

where f_{0a}, f_{ab} and $f_{b\infty}$ are the values of a given parameter f for the regions contained in the ranges $0 \leq x < a$, $a \leq x \leq b$ and $x > b$, respectively. For this model, the parameter f as a function of the implantation energy E, $f(E)$ is calculated as:

$$f(E) = p_{0a}(E)f_{0a} + p_{ab}(E)f_{ab} + \int_b^c P(x,E)f(x)dx + p_{c\infty}(E)f_{c\infty} \tag{2.23}$$

The algorithm is implemented in MATLAB, and calculates a theoretical $f(E)$ as previously described. For this, initial values for all the parameters - a, b, f_{0a}, f_{ab} and $f_{b\infty}$ - are required, inferred from a visual inspection of the experimental data.

Nextly, the Fminuit routine is used to fit $f(E)$ to the experimental points. Fminuit is a program developed for MATLAB by G. Allodi based on the Minuit minimization routine used at CERN [All10; JW04].

The application of the DREAM routine to the μSR data obtained for Al_2O_3/CIGS is plotted in fig. 2.12 and fig. 2.13. The fitting procedure was applied to the relaxation rate λ and to the effective field, $B_{eff} = \frac{\omega}{\gamma_\mu}$. The first layer thickness results obtained from the fit to the function $f(E)$ are in table 2.3.

	λ (μs^1)	B_{eff} (mT)
1^{st} layer thickness (nm)	22(1)	24(3)
χ^2	1.4	1.1

Table 2.3: Fitting values and reduced χ^2 obtained for the analysis of the relaxation rate (λ) and effective field (B_{eff}) as a function of the implantation energy (fig. 2.12).

The values obtained for the first layer thickness for both μSR parameters are consistent with the thickness measured by TEM.

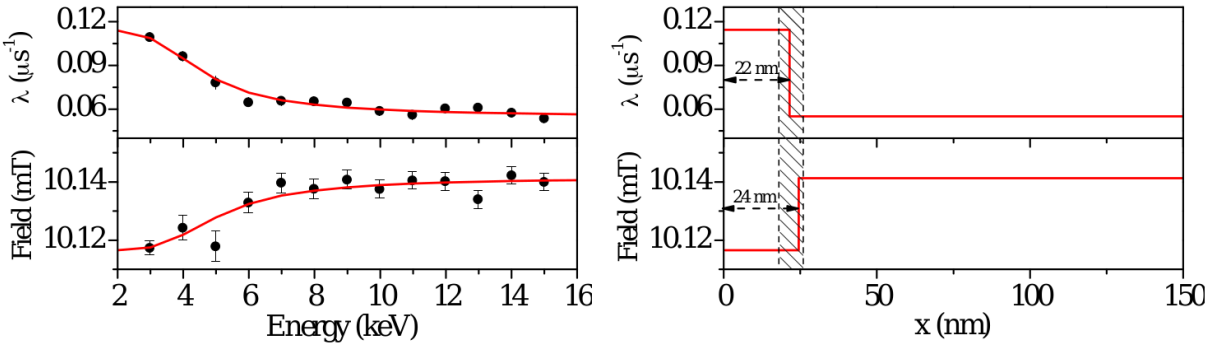

Figure 2.12: Left: Plot of the experimental data for the relaxation rate (λ) and effective field (B_{eff}) as a function of the implantation energy and respective fit to $f(E)$. **Right:** Step function $f(x)$ result for the relaxation rate (λ) and effective field (B_{eff}) as a function of implantatio depth x. The shaded region is the interface between Al_2O_3 and CIGS has measured by TEM. (from [Sim+20])

For the diamagnetic fraction f_{dia} three distinct fits to the experimental data were tested: two steps, three steps and three steps with smooth transition. The thickness of the first layer obtained for these three methods is in table 2.4

	Diamagnetic Fraction (%)		
	(a)	(b)	(c)
1^{st} layer thickness (nm)	31(4)	22(1)	18(2)
χ^2	3.4	1.6	1.7

Table 2.4: Fitting parameters and reduced χ^2 obtained for the analysis of the diamagnetic fraction (f_{dia}) as a function of the implantation energy (fig. 2.12).

The f_{dia} fit to a two steps function has a result for the first layer thickness outside the acceptance region (22 ± 4) nm and an associated $\chi^2 = 3.6$, which means this presents a poor description of the data. Regarding fig. 2.13(b), the fit quality has increased with the addition of a third step. The final fit, with a smooth transition between the second and third regions does not show an improvement relative to the previous fit. It is nevertheless important to mention that the author points that this smoothing fit is probably closer to the real behavior of the interface.

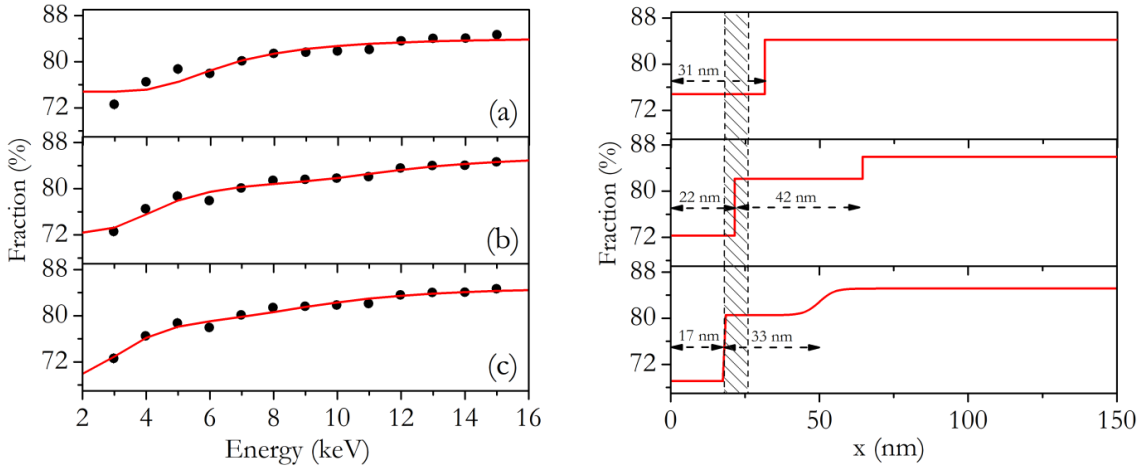

Figure 2.13: Left: Diamagnetic fraction as a function of muon implantation energy, f_{dia} at T=40 K. The red curves are the predicted behavior of the parameter assuming a depth dependence, $f_{dia}(x)$. **Right:** Diamagnetic fraction as a function of implantation depth, $f_{dia}(x)$. (a): fit to a two step function, (b): fit to three regions, (c): three regions are considered with a smooth transition. The shaded region is the interface between Al_2O_3 and CIGS has measured by TEM. (from [Sim+20])

This article demonstrates the importance of a depth resolved tool in the analysis of slow-μSR data: slow muon implantation measurements, and the successful application of DREAM in the study of semiconductors with μSR. However, this method is not limited by the choice of material and is useful to study a variety of experimental parameters, such as the effective field, diamagnetic fraction and relaxation rate.

Most recently, the data in [Alb+18] were reanalyzed in [Rib+20]. In the former study, slow μSR data were acquired for CIGS with two distinct buffer layers. As stated ZnSnO can be be a good Cd-free alternative to CdS, the most used as the n-type material in CIGS based solar cells. Therefore, this study was focused on comparing the effect each buffer layer had on CIGS, using the depth resolved analysis provided by the recently developed algorithm.

The diamagnetic signal time spectra was fitted to a Gaussian-damped oscillation to the Larmor muons frequency (eq. (2.8)).

Figure 2.14 and fig. 2.15 show the depth resolved analysis performed for parameters f_{dia} and σ. The samples shown are the heterostructures CdS/CIGS, ZnSnO/CIGS and the bulk CIGS sample.

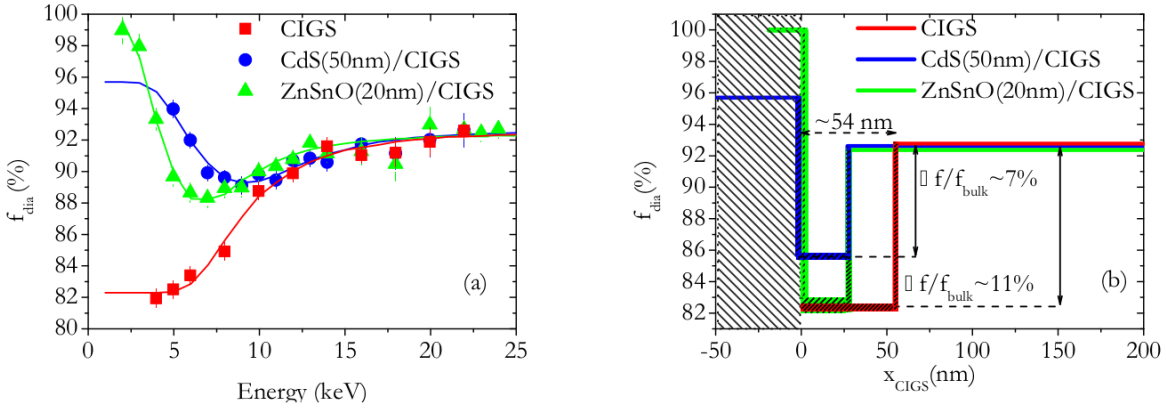

Figure 2.14: Left: Plot of the diamagnetic fraction as a function of the implantation energy $f_{dia}(E)$=50K. The curves are the fit obtained and the points correspond to the experimental data. **Right:** Fit of the diamagnetic fraction as a function of CIGS implantation depth (x_{CIGS}). The thickness of the lines represent the uncertainties. (from [Rib+20])

The main observation is the dip in the diamagnetic fraction at the interface in the heterostructures and at the CIGS surface. This effect is attributed to the surface defect layer being the extent ($\sim$ 54 nm) of the affected region is attributed to the length of the surface defect layer on bare CIGS. Previous reports have found that the surface of CIGS is a defect-rich region due to the reduction of Cu concentration when compared to its bulk. Finally, fig. 2.14 allows for a better comparison between the healing effect each buffer has on the surface of CIGS. When the junction between the two materials is formed, a depletion region appears, and this may cause a diffusion of Cu to the inner part of the surface defect layer in CIGS, where the healing is observed. ZnSnO has the effect of reducing the dip width, when comparing to the one on the CIGS bare surface. But in CdS/CIGS both the width and the depth of the affected diamagnetic signal are reduced.

As for the Gaussian relaxation in CIGS (fig. 2.15) the higher value at the surface suggests the presence of a region with distinct composition, which changes the muon environment. This

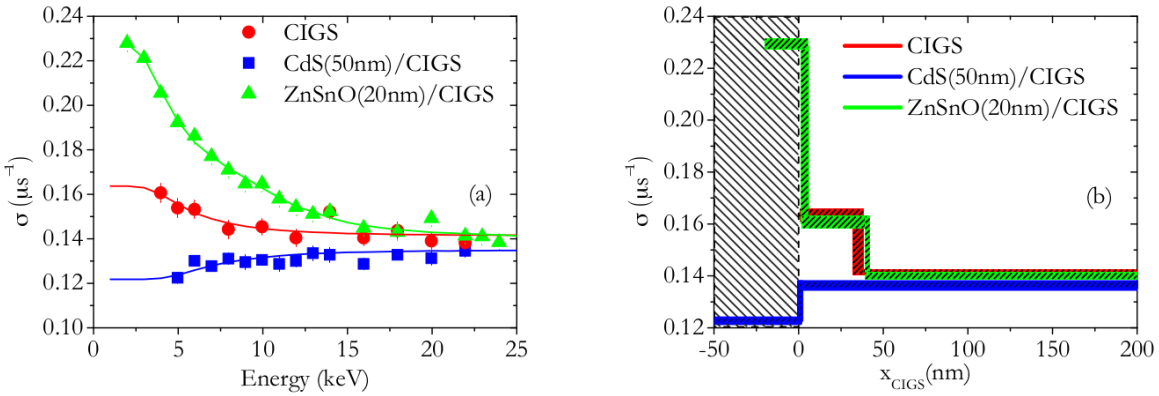

Figure 2.15: Left: Plot of the Gaussian relaxation σ as a function of the implantation energy $\sigma(E)$=50K. The curves are the fit obtained and the points correspond to the experimental data. **Right:** Fit of the relaxation as a function of CIGS implantation depth $\sigma(x_{CIGS})$. The thickness of the lines represent the uncertainties.(from [Rib+20])

can be caused by a disordered region, structural defects or electron capture. This strong relaxation region is still observed when ZnSnO is added but disappears in the presence of CdS. Such observations support the role of CdS in the surface reconstruction in CIGS, close to the p-n interface, which does not seem to occur for ZnSnO.

As for the measurements performed on CdS/Al_2O_3/CIGS, reported in [Sim19], where the study of CIGS surface passivation, there is not a significant decrease of the width of the region where the muon signal is affected. This suggests two possible effects due the insulator layer:

i. the passivation is due to defect incorporation which contribute to an increase of the surface defect layer;

ii. the width space charge region increases due to fixed charges present in the Al_2O_3.

To obtain information about the contribution of the fixed charges on the interface of CIGS, we study systems where the charge density can be controlled. As mentioned in section 1.3.7, SiO_2/CIGS samples can be produced with opposite polarity, changing the deposition conditions of the SiO_x layer. Furthermore, SiO_2/Si samples with opposite charge in the insulator layer are produced and measured, as previously mentioned.

As seen throughout the previous experiments, depth resolved analysis plays a major role in the interpretation of slow μSR data. The tool previously developed has shown to be useful for studies with semiconductor materials, and can be applied to multiple μSR parameters. Currently, the routine is only capable of fitting experimental data set at a time. Observations based on [Rib+20] show both the diamagnetic fraction and the relaxation present common fitting parameters. For example, the variation of f_{dia} and σ start at the same implantation depth. Therefore, it is of interest for further analysis, to develop the method to fit more

than one experimental parameter simultaneously, given their similar behavior as function of implantation depth.

During this work, two simultaneous fit features for DREAM are developed, while also improving the usability of the depth resolved analysis tool. The simultaneous fits are used in the analysis of the data obtained in the μSR study of the charge effect on the interface formed between SiO_2 and CIGS.

3

Results and discussion

We intend to investigate the effect of fixed charges on CIGS, as well as the effect of a dielectric layer on the passivation of SiO_2/CIGS interface.

With this goal in mind, we decided to study systems in which the charge at the interface can be controlled, using CIGS covered with SiO_2. Previous works have shown that it is possible to obtain a negative or positive charged SiO_x layer [Cun+18]. Therefore, two SiO_2/CIGS samples were measured at the Low-Energy Muon (LEM) instrument at PSI, one with a positive and the other with a negative charge at the SiO_2/CIGS interface.

Another two samples with opposite charge SiO_2 on top of Si were measured. They are used as reference since SiO_x/Si systems are more extensively studied and characterized.
Furthermore, a CIGS sample is measured to compare its behavior in bulk to the observations with a dielectric top layer with different fixed charges.

Figure 3.1: One of the samples measured at the PSI LEM instrument mounted on the sample-holder (photo from the author).

The samples measured at PSI for the purpose of this study were:

- SiO_2+/CIGS (BR1)
- SiO_2−/CIGS (TL4)
- SiO_2+/Si (BR1 Si)
- SiO_2−/Si (TL4 Si)
- CIGS film

Figures 3.2 and 3.3 provide a representation of these samples.

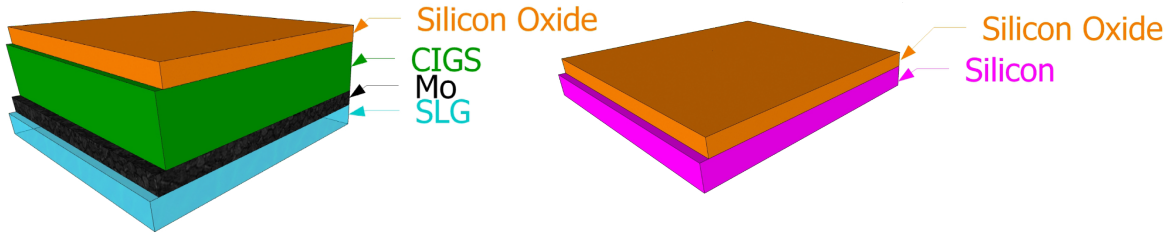

Figure 3.2: SiO_2 deposition process is PECVD. **Left:** SiO_2/CIGS sample with expected Si_2 layer thickness of 60 nm. **Right:** SiO_2/Si sample with expected SiO_2 layer thickness of 60 nm. (figure provided by Marco Alberto).

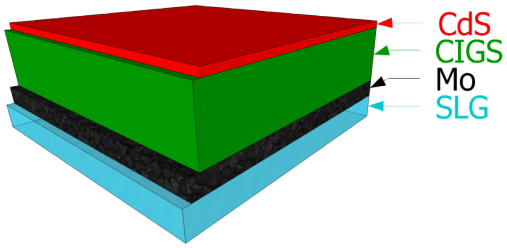

Figure 3.3: CIGS sample with CdS buffer layer which was removed to measure the bulk CIGS properties. (figure provided by Marco Alberto).

All the samples containing SiO_2 have a first dielectric layer with an expected thickness of 60 nm. Both the Si and CIGS samples with the same charge SiO_2 were simultaneously deposited. This means they are expected to have approximately the same thickness.

The samples were grown and characterized at International Iberian Nanotechnology Laboratory (INL). The samples were kept and transported to PSI in vacuum until it was time to perform the measurements, to avoid their oxidation.

The CIGS sample had a CdS coating. The CdS layer was removed by Marco Alberto from INL right before measurement by etching with a 10% (V/V) HCl solution, in order to avoid its exposure to air since it causes surface oxidation.

The deposition process of SiO_2 is plasma enhanced chemical vapor deposition (PECVD), and in [Cun+18] it was observed that different frequencies during this process resulted in samples with opposite fixed charges. Hence, the BR1 samples were deposited at a temperature T=300 °C and high field (HF) whereas the TL4 samples were produced at a temperature T=150 °C and low field (LF), and therefore they are expected to have a positive and a negative charge density, respectively.

3.1 Experimental data

All the samples were measured at the LEM instrument at a temperature T=50 K and in the presence of a transverse magnetic field B=10 mT, while varying the muon implantation energy, E, between 3 and 22 keV. As explained in section 2.1.4, the muons go through a moderation process in order to obtain low muon implantation energies. After being slowed down from 4 MeV to energies of the order of 15 eV, an electric potential difference called moderation voltage is applied in order to achieve muon implantation energies in the desired range. For the measurements with E between 3 and 16 keV, the moderation voltage is fixed at 15 kV but is increased to 16.5 kV to achieve the higher implantation energies.

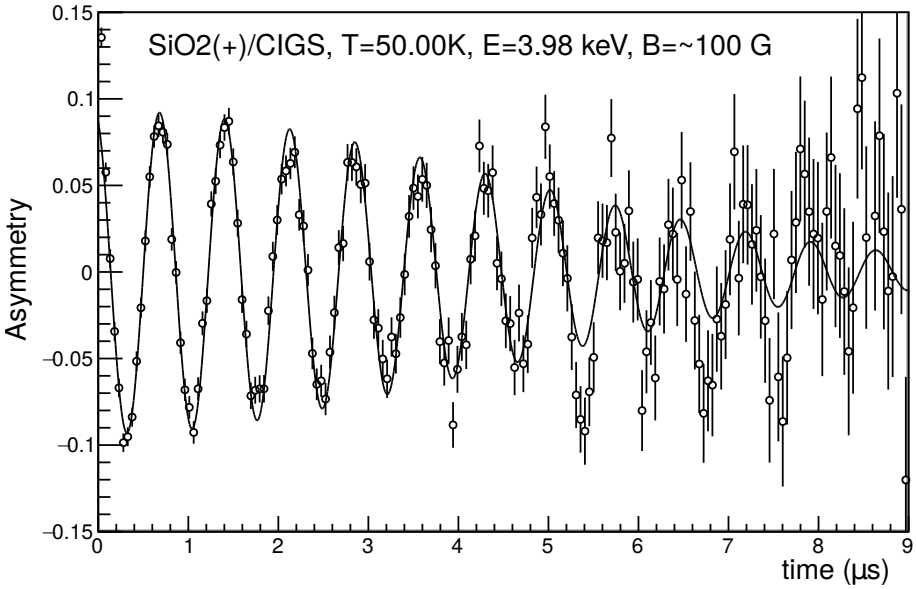

Figure 3.4: μSR spectrum measured for the SiO_2+/CIGS sample at T=50 K, with a muon implantation energy E=3.98 keV, in the presence of a transverse magnetic field B=10 mT. The fit to a Gaussian damped cosine function is represented by the line.

The preliminary data obtained over the LEM runs was analyzed using `musrfit`, which is a framework developed for μSR data analysis [SW12]. The signal obtained can be described by a one-component function, which corresponds to the muon fraction forming a diamagnetic state. The best description of the signals was obtained for all the samples when fitting them to a Gaussian damped cosine with an angular frequency ω close to the Larmor frequency:

$$A(t) = A_{dia}\, \mathrm{e}^{-\frac{1}{2}\sigma^2 t^2} \cos(\omega t + \phi) \tag{3.1}$$

which is the diamagnetic signal A variation with time t. A_{dia} is the diamagnetic signal amplitude, σ is the Gaussian spin relaxation rate, and ϕ is the phase. Therefore the analysis provides the experimental dependence of these μSR parameters like asymmetry, relaxation rate, diamagnetic fraction, field, and phase with muon implantation energy.

The fits of the preliminary data on `musrfit` were performed for a time range between 0.07 and 9 μs: before 0.7 μs the muons detected decay in flight, prior to reaching the sample, while after t=9 μs the data points have large error bars. Figure 3.4 is the signal obtained for the SiO_2/CIGS sample fitted to eq. (3.1).

The effective field at the muon is calculated through the relation in eq. (2.1), by dividing the angular frequency ω by the muon gyromagnetic ratio γ_μ as follows

$$B_{eff} = \frac{\omega}{\gamma_\mu} \tag{3.2}$$

The maximum asymmetry is obtained using a silver sample measured at the LEM at T=200 K in the presence of a transverse magnetic field B=10 mT. This is called the calibration curve, and it was measured by the LEM team for each muon implantation energy. The experimental data reveals that the asymmetry measured for all the samples is inferior to the calibration value, therefore there is a missing fraction.

To account for the effect of the muons falling on the sample plate, a nickel plate is also measured. Its asymmetry is calculated as a function of muon implantation energy E according to eq. (3.4), for a given moderation voltage.

$$A(E,\,\mathrm{Ag}) = p_0 \cdot \left[1 - \exp\left(-\frac{E}{E_0}\right)\right] + p1 \tag{3.3}$$

$$A(E,\,\mathrm{Ni}) = A_0 \cdot \exp\left(-\frac{E}{E_1}\right) + \mathrm{offSet} \tag{3.4}$$

The silver calibration curve as well as the correction parameters were provided by Dr. Thomas Prokscha. The correction parameters for moderation voltages of 15 kV and 16.5 kV are displayed in table 3.1.

Finally, the diamagnetic fraction is calculated in eq. (3.5) as the ratio between the asymmetry measured for the studied sample and the maximum Ag asymmetry, after subtracting to each one the contribution of muons stopping on the sample plate.

Moderator HV (kV)	p_0	p_1	A_0	E_1	offset
15	0.0863(58)	0.1432(51	0.100(14)	1.83(22)	0.0095(10)
16.5	0.1055(85)	0.1370(78)	0.072	2.28	0.132

Table 3.1: Correction parameters for moderation voltages of 15 and 16.5 kV used in the calculation of diamagnetic fraction.

$$f_{dia}(E) = \frac{A(E,\,\mathrm{sample}) - A(E,\,\mathrm{Ni})}{A(E,\,\mathrm{Ag}) - A(E,\,\mathrm{Ni})} \tag{3.5}$$

The diamagnetic fraction was calculated using a ROOT macro C++ program, provided by Dr. Thomas Prokscha, which implements the corrections previously described. The program reads the files generated when fitting the raw data with `musrfit` and performs the calculations of diamagnetic fraction f_{dia} and its associated error.

The asymmetry, diamagnetic fraction, relaxation rate, effective field at the muon, and phase obtained as a function of muon implantation energy for the sample SiO_2-/CIGS measured at the LEM are represented in figs. 3.5 to 3.9. The μSR parameters depicted are a result of the `musrfit` analysis.

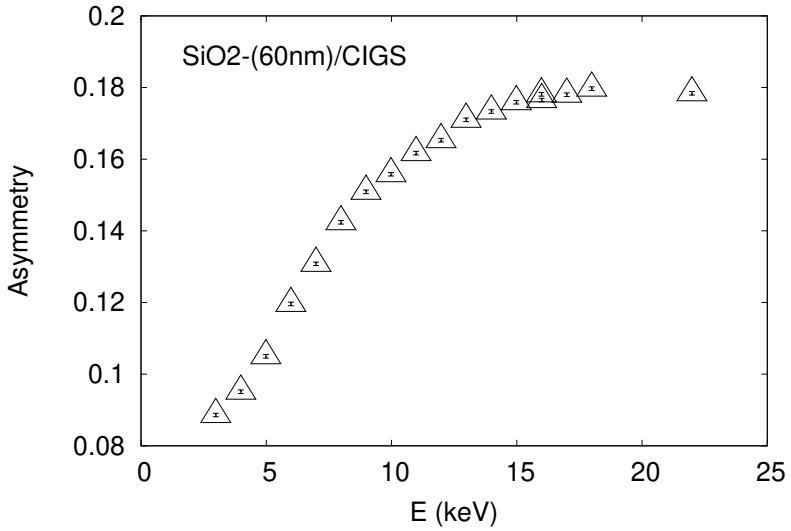

Figure 3.5: Asymmetry as a function of muon implantation energy E measured at a temperature T=50 K in the presence of a transverse field B=10 mT. Energy measurements performed between 2 and 16 keV used a moderation voltage equal to 15 kV whereas above an energy E=16 keV the voltage was 16.5 kV.

For an implantation energy of about 16 keV two points are measured, one with a moderation voltage of 15 kV and the other 16.5 kV. After turning this voltage to 16.5 kV the measured values display a small downward shift. The effect is most evident for the diamagnetic fraction (fig. 3.6), which is sensitive to the muon beam alterations caused by the voltage applied in the moderator.

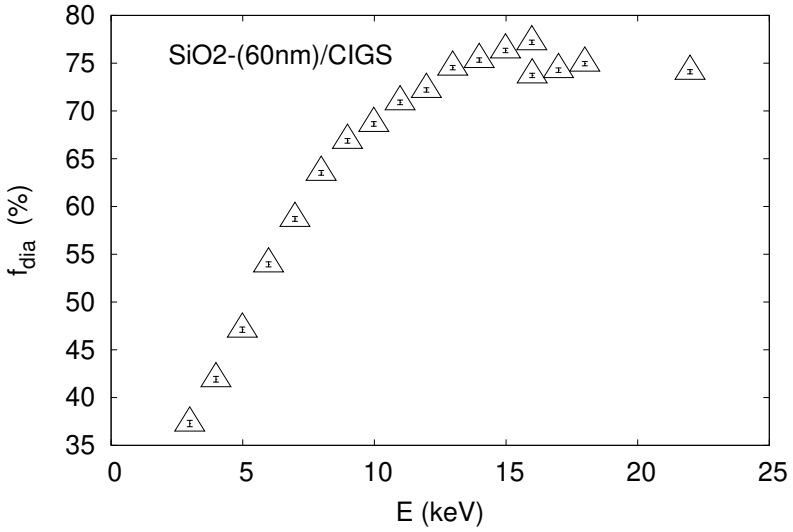

Figure 3.6: Diamagnetic fraction f_{dia} as a function of muon implantation energy E measured at a temperature T=50 K in the presence of a transverse field B=10 mT. Energy measurements performed between 2 and 16 keV used a moderation voltage equal to 15 kV whereas above an energy E=16 keV the voltage was 16.5 kV.

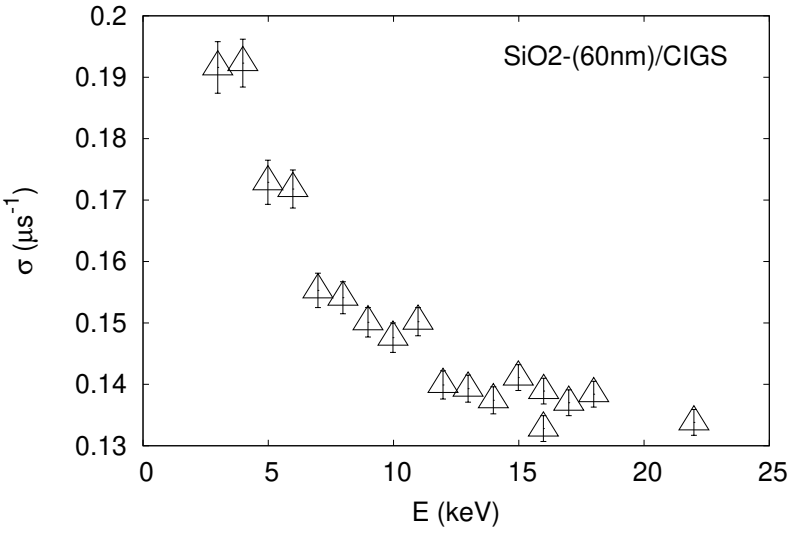

Figure 3.7: Spin relaxation rate σ as a function of muon implantation energy E measured at a temperature T=50 K in the presence of a transverse field B=10 mT. Energy measurements performed between 2 and 16 keV used a moderation voltage equal to 15 kV whereas above an energy E=16 keV the voltage was 16.5 kV.

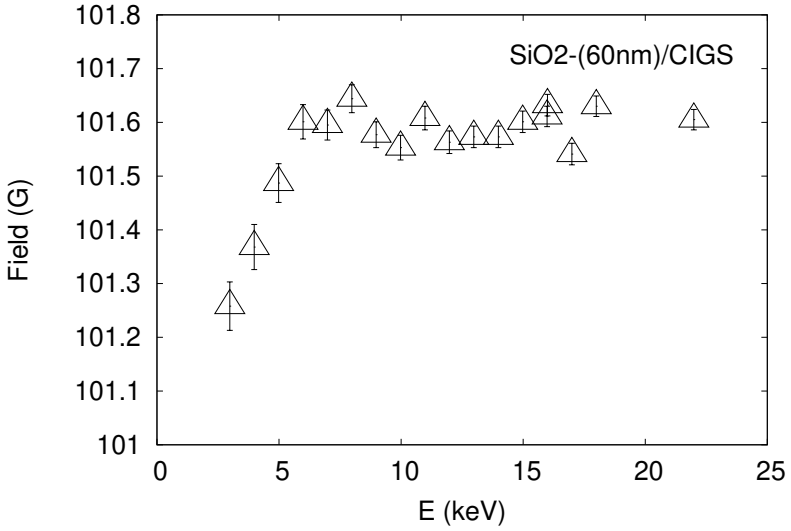

Figure 3.8: Effective field at the muon as a function of muon implantation energy E measured at a temperature T=50 K in the presence of a transverse field B=10 mT. Energy measurements performed between 2 and 16 keV used a moderation voltage equal to 15 kV whereas above an energy E=16 keV the voltage was 16.5 kV.

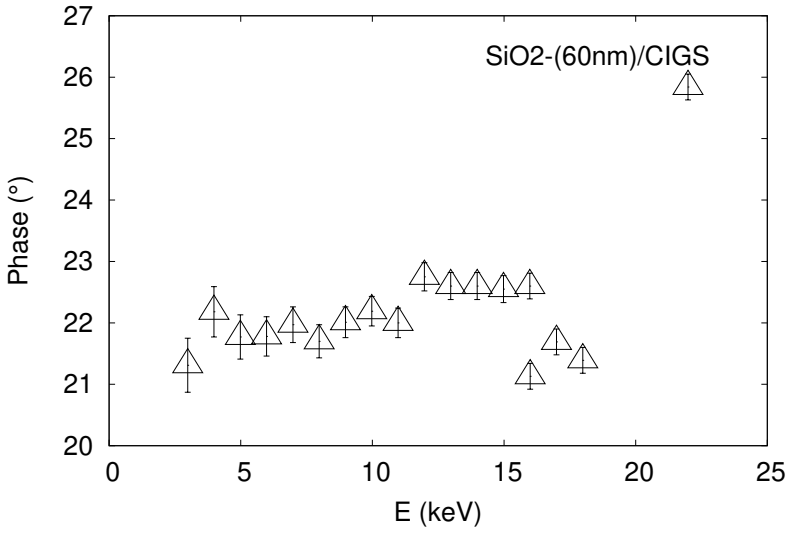

Figure 3.9: Phase as a function of muon implantation energy E measured at a temperature T=50 K in the presence of a transverse field B=10 mT. Energy measurements performed between 2 and 16 keV used a moderation voltage equal to 15 kV whereas above an energy E=16 keV the voltage was 16.5 kV.

3.2 Depth resolved analysis

The previous work addressed in section 2.2.2 shows the utility of depth resolved analysis tool DREAM in the study of thin-films and multi-layered structures. DREAM is a MATLAB program first developed by Simões, which uses the Fminuit software based on the MINUIT minimization engine from CERN [All10; JW04].

As previously mentioned, the μSR parameters are obtained as a function of muon implantation energy, and with variation of energy we can achieve different implantation depths. The main feature of DREAM is that it obtains the relation of the μSR parameters with the muon implantation depth based on the stopping probability per unit length $P(x,E)$ that a muon implanted with energy E stops at a depth x. We get $P(x,E)$ by running a Monte Carlo simulation TRIM.SP [Mor+02] for each studied sample. Figures 3.10 and 3.11 represent $P(x,E)$ obtained for SiO_2/CIGS and SiO_2/Si for various implantation energies, respectively.

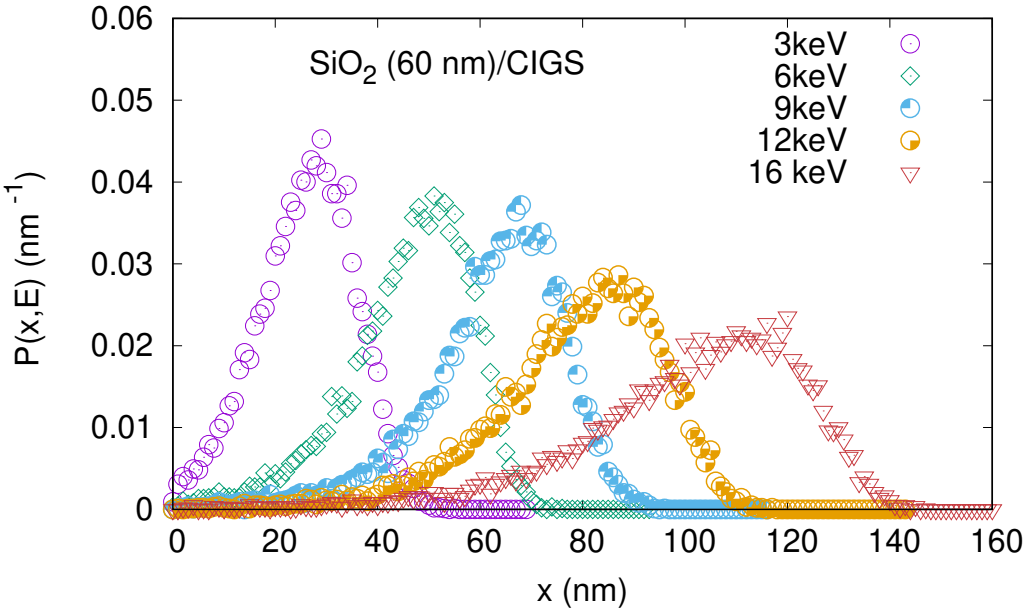

Figure 3.10: Stopping probability $P(x,E)$ that a muon implanted with an energy E stops inside the sample at depth x. The values represented are obtained with using Monte Carlo simulation TRIM.SP for a sample of CIGS with a top layer of amorphous SiO_2 with a thickness of 60 nm. The different colors represent the muon implantation energies. For a muon implantation energy E=16 keV, $P(x,E)$ has a maximum at about 120.5 nm, which corresponds to an average implantation depth 60 nm inside the CIGS layer.

For a muon implantation energy E=16 keV, the maximum depth the muons can probe inside SiO_2/CIGS and SiO_2/Si is between 120 and 130 nm, as the distributions in Figures 3.10

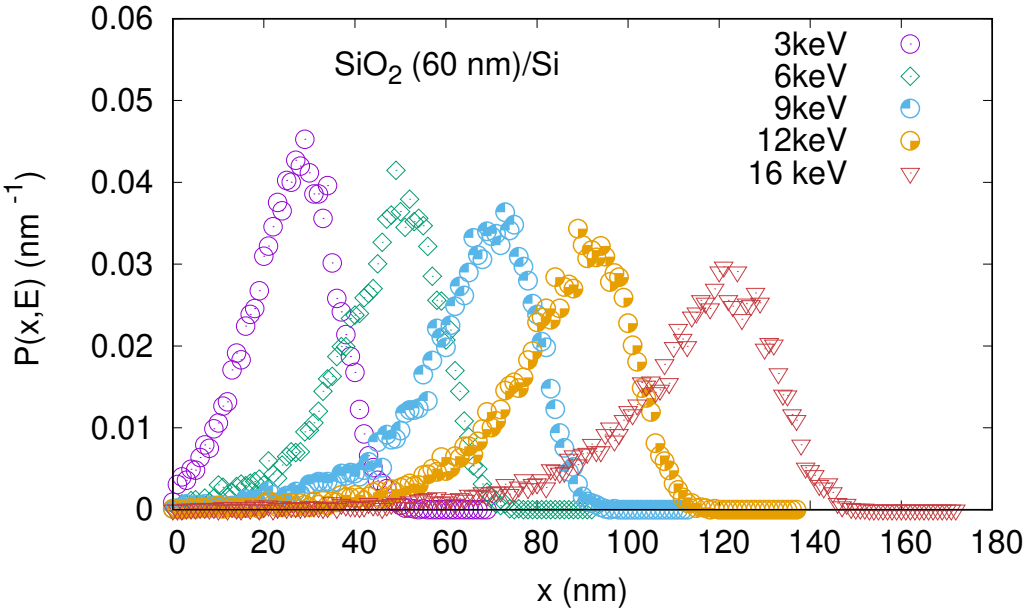

Figure 3.11: Stopping probability $P(x,E)$ that a muon implanted with an energy E stops inside the sample at depth x. The values represented are obtained with using Monte Carlo simulation TRIM.SP for a sample of Si with a top layer of amorphous SiO_2 with a thickness of 60 nm. The different colors represent the muon implantation energies. For a muon implantation energy E=16 keV, $P(x,E)$ has a maximum at about 124.5 nm.

and 3.11 show.

The analysis of this work will be focused on the experimental data of diamagnetic fraction f_{dia} and relaxation rate σ, as these parameters provide the most information about the effect of different fixed charges on CIGS. The experimental variation of the μSR parameters with muon implantation energy was measured for E between 3 and 22 keV. However, we decided to include only the data obtained for energies under 16 keV, not considering the values affected by the alteration of the moderator voltage in order to avoid misleading experimental artifacts.

The first analysis was performed using the version 1.10 of DREAM, described in section 2.2.2 and will be presented next. The χ^2 obtained for the fits had considerably big values, which we attributed to the underestimation of the errors associated to the μSR parameters. Therefore, we will use visual evaluation to establish the appropriate fits.

Diamagnetic fraction

In an initial analysis, we considered a description of diamagnetic fraction as a function of muon implantation depth $f_{dia}(x)$ that followed the observations in the study of amorphous SiO_2 using μSR in [Pro+07]. Its results showed a decrease of diamagnetic states formation

with increasing energy. Therefore we tried fitting the experimental $f_{dia}(E)$ data assuming $f_{dia}(x)$ has a first region, inside the first layer of SiO_2, that can be described by a linear function with negative variation.

The first step in testing this approach was to obtain the slope of $f_{dia}(x)$ for the amorphous SiO_2 based on the energy dependence measured in [Pro+07] using DREAM (fig. 3.12). The fraction here is measured for about the same muon implantation energy (2 to 20 keV) as in our study, therefore we can assume we are seeing the same depth inside SiO_2 in both cases. The slope obtained for the linear variation in the first region of $f_{dia}(x)$ is $-0.3223\,\mathrm{nm}^{-1}$. This value was thereafter used to implement the approach on all samples containing a top layer of SiO_2. The fits obtained for the SiO_2/CIGS samples is presented as example in fig. 3.13.

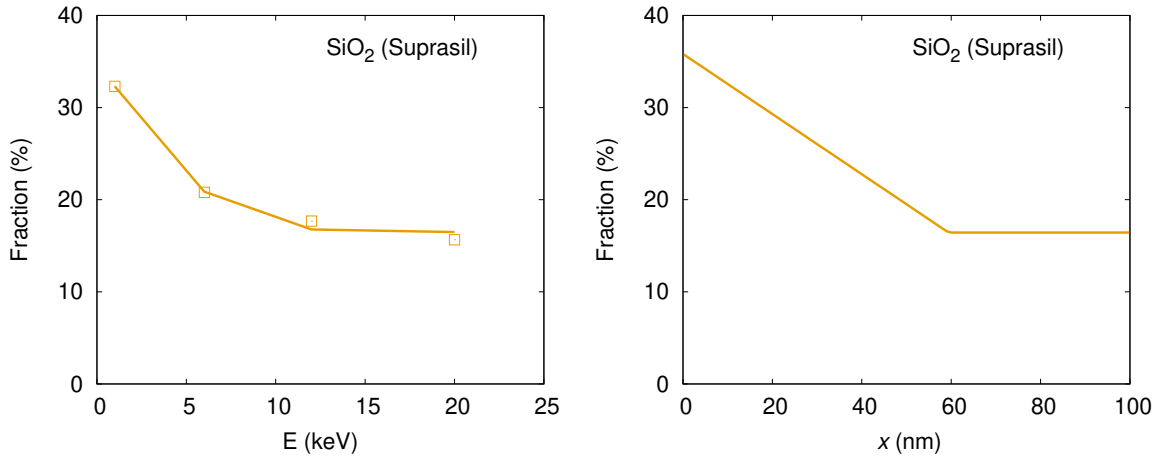

Figure 3.12: Left: Diamagnetic fraction as a function of muon implantation energy taken from [Pro+07]. The curve represents the predicted behavior of the $f_{dia}(E)$ when assuming a depth dependence as shown on the corresponding graph on the right. **Right:** The variation of diamagnetic fraction as a function of muon implantation depth, $f_{dia}(x)$, described by a linear decrease with a slope of $-0.3223\,\mathrm{nm}^{-1}$ followed by a constant value.

The observation of fig. 3.13 denotes that two regions are not sufficient to obtain a good description of experimental data, so an intermediate step is added and we assume a description with three regions for both SiO_2+ and SiO_2- samples. The addition of a third step significantly improves the description, but suggests the presence of an interface region that starts inside the SiO_2 layer and ends within CIGS. This can be taken as an indicator of intermixing at the interface, since we are not observing the expected behavior inside SiO_2 most likely due to the effect of the heterojunction formed between SiO_2 and CIGS.

The fits in fig. 3.13 also raise the question whether within the first region in SiO_2 we can distinguish between a linear and constant behavior of $f_{dia}(x)$. Therefore we tested fitting $f_{dia}(E)$ assuming a $f_{dia}(x)$ dependence described by a step function. This follows the work summarized in sections 2.2.1 and 2.2.2, where a sample is a multi-layered system, and within each

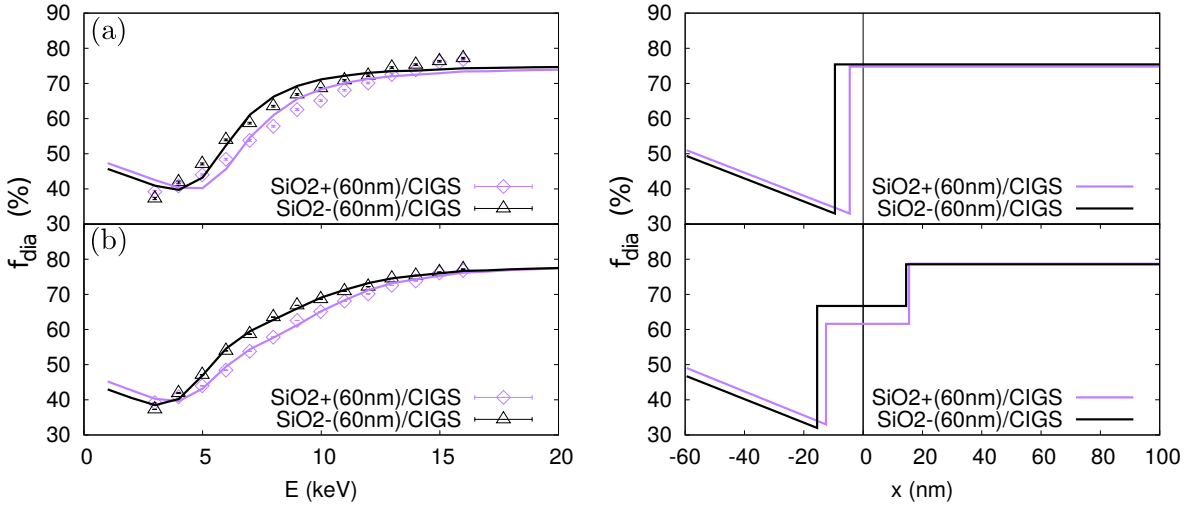

Figure 3.13: Left: Experimental data of diamagnetic fraction as a function of muon implantation energy for SiO2(+)/CIGS (purple) and SiO2(-)/CIGS (black) samples. The curves represented show the predicted behavior of f_{dia} considering an implantation depth dependence as shown on the corresponding graph to the right. **Right:** Diamagnetic fraction as a function of implantation depth, $f_{dia}(x)$ fitted to: **(a)** two regions and **(b)** three regions. The first region of $f_{dia}(x)$ is assumed to have a linear decrease followed by one (a) or two (b) regions where f_{dia} is constant.

layer the μSR parameter f is constant. Considering, for example, the sample SiO_2+/CIGS it is expected that its $f(x)$ has at least two regions, each one with the characteristic value of the layer material, i.e. the first would have SiO_2 f typical value, and the second region the characteristic value of CIGS. However, some samples exhibit a variation of f within the layer, typically close to the interface of two material or at the surface, the latter case is observed for CIGS [Alb+18]. This analysis provides information about the extension of each layer, and in particular about the regions affected by the interface.

The result of this approach for $SiO_2(+/-)$/CIGS is represented in fig. 3.14. The fit to a two step function did not offer a good description of the experimental data, as one can see. Hence, a third region is placed as an intermediate step, which is located at the sample interface, for both cases. Visually, we can determine that assuming a three step function for $f_{dia}(x)$ provides a better description for $f_{dia}(E)$. Comparing the results obtained in fig. 3.13(b) and fig. 3.14(b) using three regions, the conclusion is that the final fitting description is similar except for very low energies (under 3 keV), for which no experimental data is available. Thus, we do not have experimental information to distinguish between the two solutions and we will adopt the simplest model of a step-like function (fig. 3.14)(b).

The experimental data $f_{dia}(E)$ belonging to the CIGS film sample is also fitted considering its depth dependence can be represented by a two steps function in fig. 3.14. For the CIGS, we see a surface region where there is a lower diamagnetic fraction. This agrees with previous data obtained with μSR in which the surface f_{dia} value is lower then in the bulk of CIGS film

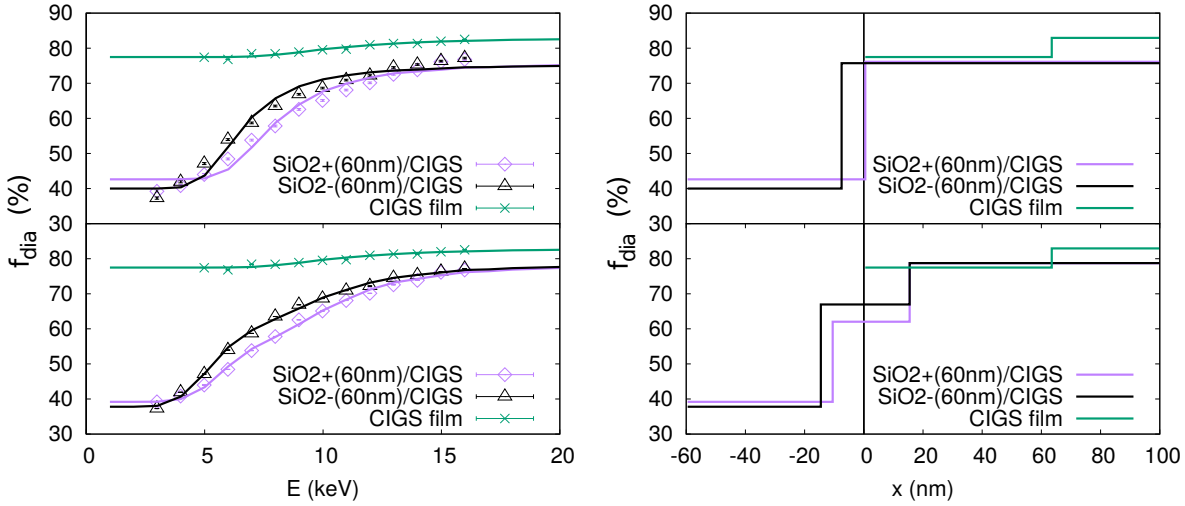

Figure 3.14: Left: Experimental data of diamagnetic fraction as a function of muon implantation energy for SiO2(+)/CIGS (purple), SiO2(-)/CIGS (black) and CIGS film (green) samples. The curves represented show the predicted behavior of f_{dia} considering an implantation depth dependence as shown on the corresponding graph to the right. **Right:** Diamagnetic fraction as a function of implantation depth, $f_{dia}(x)$ fitted to **(a)** two steps and **(b)** three steps function.

[Alb+18; Rib+20]. Interestingly, the value obtained in SiO_2/CIGS at the largest implantation energies is still below the bulk value measured in CIGS film. This suggests that in SiO_2/CIGS we never reach the bulk CIGS region.

Relaxation rate

In a preliminary fit of relaxation rate σ as a function of muon implantation energy E, the experimental data of each sample containing CIGS was fitted assuming σ variation with implantation depth as a two steps function. For SiO_2+ and SiO_2- samples a second fit of this parameter was performed, this time assuming a $\sigma(x)$ fit to a three steps function. The fits obtained are in fig. 3.15.

The intermediate step we can observe when adding a third step happens at the interface of SiO_2 and CIGS for both positive and negative charged samples, and occurs at approximately the same depth as the middle step in $f_{dia}(x)$ (in fig. 3.14). We consider this description to provide the best fit for $\sigma(x)$.

As for the CIGS film, two steps are needed to describe the relaxation rate of inside this sample, as there is a surface region where σ is higher than the bulk characteristic value.

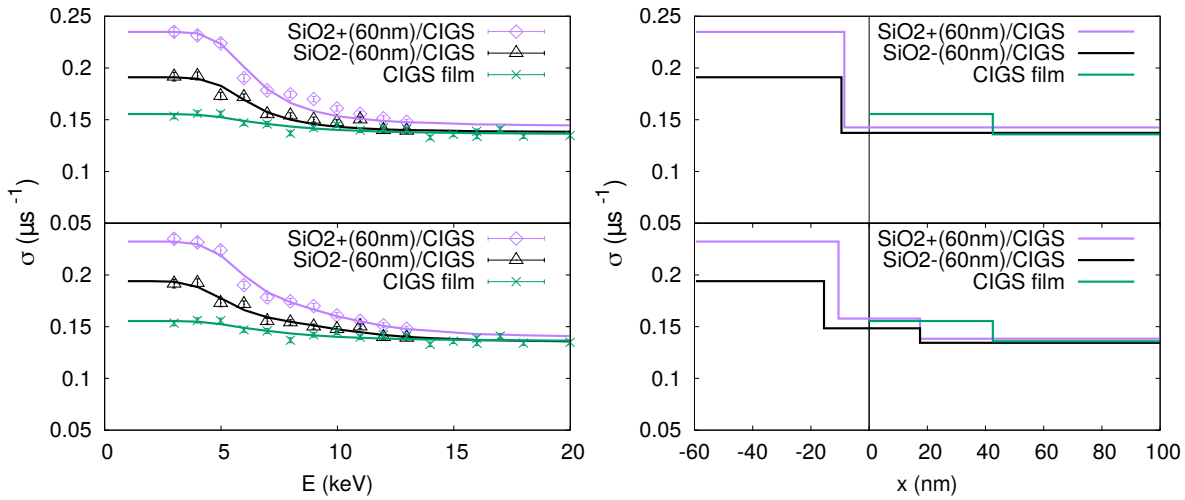

Figure 3.15: Left: Experimental data of relaxation rate σ as a function of muon implantation energy E for SiO2(+)/CIGS (purple), SiO2(-)/CIGS (black) and CIGS film (green) samples. The curves represented show the predicted behavior of σ considering an implantation depth dependence as shown on the corresponding graph to the right. **Right: (a)** Relaxation rate as a function of implantation depth, $\sigma(x)$ fitted to a two regions for all samples containing CIGS. **(b)** Relaxation rate as a function of implantation depth, $\sigma(x)$ fitted to a three steps function for SiO2(+/-)/CIGS samples. The two steps description of CIGS is also displayed.

3.3 Simultaneous fits using DREAM

All the depth resolved analysis presented so far was obtained using DREAM to fit each data set. As previously discussed, this program can be further enhanced in order to increase its power and usability, this means adding new features to the tool while making it easily accessible. With this in mind, a simultaneous fit feature is developed, tested and applied in the study of $SiO_2(+/-)$/CIGS and $SiO_2(+/-)$/Si samples. Although, allowing simultaneous fits was the main focus of this work, the program also made progress in the way data is introduced and saved, and simplified these processes for the new and existing features. The instructions manual with an illustrated example can be found in Appendix A.

When we say we can perform a simultaneous fit using DREAM it means the program is capable of fitting two data sets at the same time using some common parameters in the data sets. This proves to be most useful in the study of multi-layered samples, like the ones in this work.

There are two cases where we can benefit from applying the simultaneous fit, and they will be discussed in detail in the following sections. The first case takes the data sets of two different μSR parameters, measured for a sample, on the assumption that the depth variations will occur at the same region. The second case performs a simultaneous fit of two data sets of a μSR parameter f measured for two different samples with at least a same type layer. Inside this layer, f is expected to have a characteristic value, therefore it is used as the common fitting parameter.

3.3.1 Simultaneous fit within the same sample

As we have noted in the first step function fits performed for $f_{dia}(x)$ and $\sigma(x)$ figs. 3.14 and 3.15, the transition between the first and second regions seems to happen at around the same depth. This can indicate the presence of a region in which the μSR parameter has a value between those of the first and second layer.

Because the values of f_{dia} and σ vary according to the material composition we can assume that the transition between steps happens at around the same depth. In terms of the depth resolved analysis, these assumptions lead us to the possibility of performing a simultaneous fit to two sets of experimental data: $f_{dia}(E)$ and $\sigma(E)$.

We will now go over the implementation of a simultaneous fit on the analysis of the two CIGS samples with SiO_2+ and SiO_2- top layer, adopting the simplest description for $f_{dia}(x)$ and $\sigma(x)$, which is a fit to a two steps function. Remembering eq. (2.20), the step function

becomes:

$$f(x) = \begin{cases} f_{0a} \text{ for } 0 \leq x \leq a, \\ f_{a\infty} \text{ for } x > a \end{cases} \tag{3.6}$$

where f_{0a} is the value of the μSR parameter in the first region for a depth x between 0 and a and $f_{a\infty}$ is the value in the second region after a depth $x = a$. We are considering $f_{dia}(x)$ and $\sigma(x)$ have equal first layer thickness, which translates in having the same a. The remaining fit parameters, f_{0a} and $f_{a\infty}$, will have different values for f_{dia} and σ. The resulting fit is represented in fig. 3.16. As expected, from the previous fit in fig. 3.14, a two steps description of $f_{dia}(x)$ does not offer a good representation of $f_{dia}(E)$, therefore we should add an intermediate step, as shown in fig. 3.17.

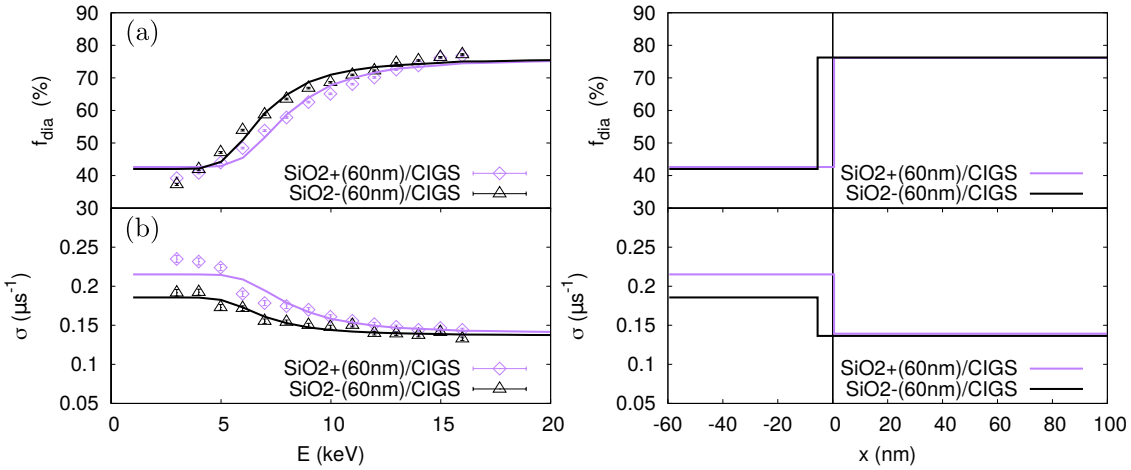

Figure 3.16: Left: Simultaneous fit of $f_{dia}(E)$ and $\sigma(E)$ for each sample, SiO_2+/CIGS (purple) and SiO_2−/CIGS (black). The curves the expected behavior of each μSR parameter assuming a corresponding depth dependence as shown on the graph on the right. **Right:** Fit of **(a)** $f_{dia}(x)$ and **(b)** $\sigma(x)$ to a two steps function. The transition between the first and second region of f_{dia} and σ is assumed to occur at the same depth for a given sample.

The simultaneous fits in figs. 3.17 to 3.19 follow the same assumption that, for a given sample, $f_{dia}(x)$ and $\sigma(x)$ have a transition between layers happening at the same depth.

In fig. 3.17 $\sigma(x)$ is fitted to a two steps function, and the overall simultaneous fit is better than in fig. 3.16. However, the preliminary fits from fig. 3.15 lead us to conclude that fitting $\sigma(x)$ to a three steps function provides a more adequate description of the experimental $\sigma(E)$. Hence, in figs. 3.18 and 3.19, both $f_{dia}(x)$ and $\sigma(x)$ are fitted to a three steps function. This means there is a second region for $a < x < b$, being that a is always assumed to be a common parameter for both $f_{dia}(x)$ and $\sigma(x)$. As for b, the upper limit of the intermediate region, it is considered to be common in fig. 3.19, but not in fig. 3.18.

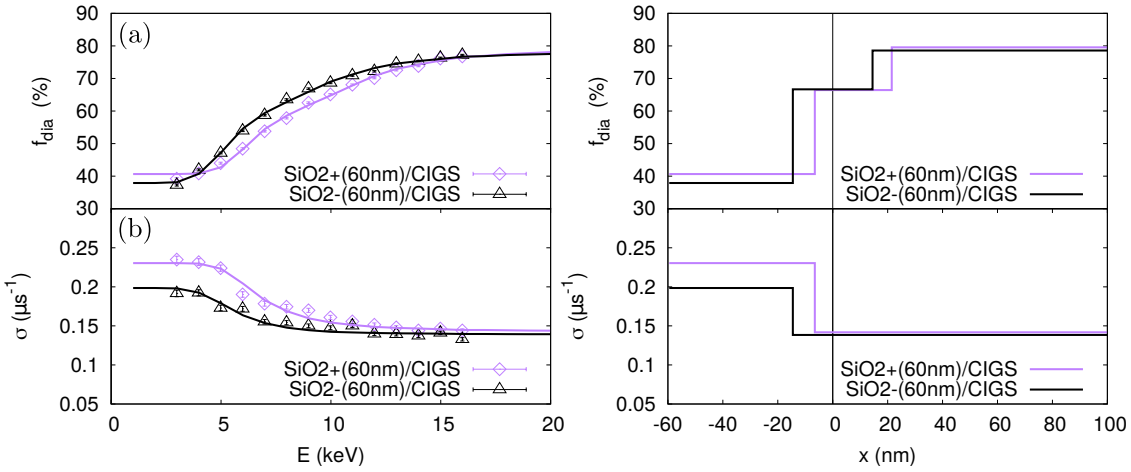

Figure 3.17: Left: Simultaneous fit of $f_{dia}(E)$ and $\sigma(E)$ for each sample, SiO_2+/CIGS (purple) and SiO_2−/CIGS (black). The curves the expected behavior of each μSR parameter assuming a corresponding depth dependence as shown on the graph on the right. **Right:** Fit of **(a)** $f_{dia}(x)$ to a three steps function and **(b)** $\sigma(x)$ to a two steps function. The transition between the first and second region of f_{dia} and σ is assumed to occur at the same depth for a given sample.

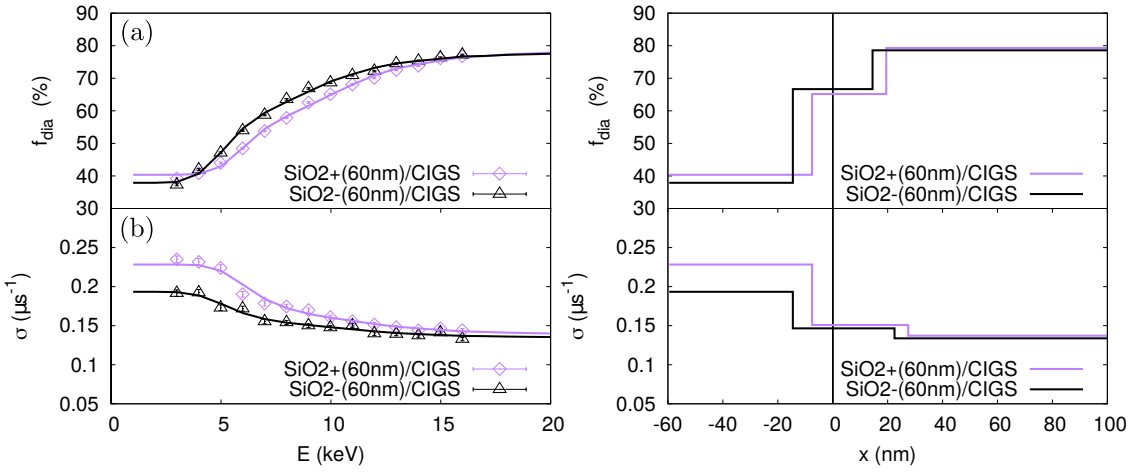

Figure 3.18: Left: Simultaneous fit of $f_{dia}(E)$ and $\sigma(E)$ for each sample, SiO_2+/CIGS (purple) and SiO_2−/CIGS (black). The curves the expected behavior of each μSR parameter assuming a corresponding depth dependence as shown on the graph on the right. **Right:** Fit of **(a)** $f_{dia}(x)$ and **(b)** $\sigma(x)$ to a three steps function. The transition between the first and second region of f_{dia} and σ is assumed to occur at the same depth for a given sample.

The observations of the simultaneous fits support the need to use a three regions description for both $f_{dia}(x)$ and $\sigma(x)$ in the case of the bilayer structures containing CIGS.

When comparing figs. 3.18 and 3.19 both parameters appear to be adequately described. However, they differ in terms of the transitive value for the transition between the second

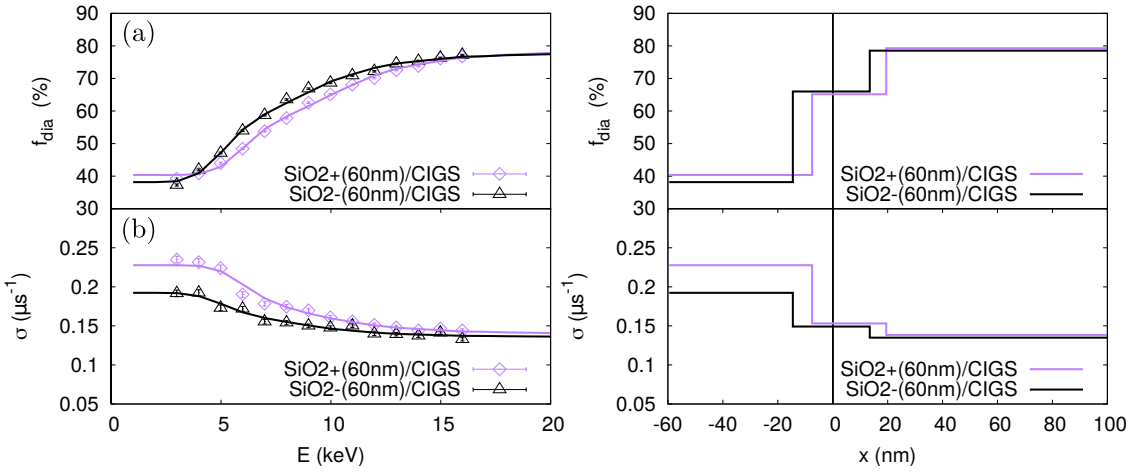

Figure 3.19: Left: Simultaneous fit of $f_{dia}(E)$ and $\sigma(E)$ for each sample, SiO_2+/CIGS (purple) and SiO_2−/CIGS (black). The curves the expected behavior of each μSR parameter assuming a corresponding depth dependence as shown on the graph on the right. **Right:** Fit of **(a)** $f_{dia}(x)$ and **(b)** $\sigma(x)$ to a three steps function. The second of region of $f_{dia}(x)$ and $\sigma(x)$ is assumed to start and end at the same depth, for each sample.

			1st layer (nm)	2nd layer (nm)
SiO_2+/CIGS	fig. 3.18	$f_{dia}(x)$	52(1)	79(1)
		$\sigma(x)$		87(2)
	fig. 3.19	$f_{dia}(x)$	53(1)	80(4)
		$\sigma(x)$		
SiO_2−/CIGS	fig. 3.18	$f_{dia}(x)$	45(1)	74(1)
		$\sigma(x)$		83(7)
	fig. 3.19	$f_{dia}(x)$	45(1)	74(1)
		$\sigma(x)$		

Table 3.2: Depth fitting parameters obtained in the depth-resolved analysis of SiO_2+/CIGS and SiO_2+/CIGS. The diamagnetic fraction $f_{dia}$and relaxation rate σ of each sample were simultaneously fitted as showed in figs. 3.18 and 3.19.

and third region, as we can see in table 3.2.

3.3.2 Simultaneous fit of different samples

The second type of simultaneous fit is to be performed for the analysis of data of two different samples which have at least a layer of the same type. The materials being studied have a characteristic value for at least a μSR parameter f, which is taken as a common parameter in the fitting procedure. Therefore, in these circumstances, we can fit two sets of data $f(E)$ at the same time assuming $f(x)$ has at least one region where its value is common to both samples.

3.3.2.1 SiO_2+/CIGS and SiO_2-/CIGS

We will now apply this simultaneous analysis to the study of diamagnetic fraction f_{dia} measured for SiO_2+/CIGS and SiO_2-/CIGS. We will go directly to fitting the dependence of f_{dia} with implantation depth x to a function with three steps, as we have seen it is the best description.

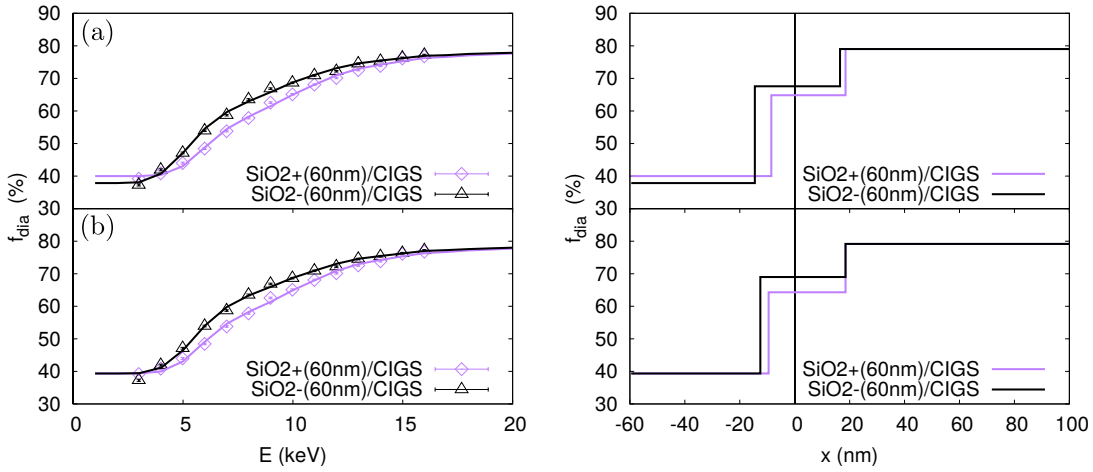

Figure 3.20: Left: The curves represent the predicted behavior of $f_{dia}(E)$ assuming a corresponding depth dependence as shown on the graph on the right for SiO_2+/CIGS (purple) and SiO_2-/CIGS (black). **Right: (a)** Simultaneous fit of $f_{dia}(x)$ assuming a fit to a three step function in which the final step value is equal for both samples. **(b)** Simultaneous fit of $f_{dia}(x)$ assuming a fit to a three step function in which the initial and final step values are equal for both samples.

Inside the CIGS layer we expect the μSR parameter to have the same value for all samples. Therefore we start by considering the final value of f_{dia} the common parameter in the simultaneous fit. The experimental data of f_{dia} as function of muon implantation energy also suggests that the first region of $f_{dia}(x)$ could have a common value for both samples, as the SiO_2+ and SiO_2- have similar initial values. In fig. 3.20 two fits are performed, the first

assuming only the final f_{dia} value to be common, and a second one where both the initial and final f_{dia} values are taken as common parameters for the two samples.

In the simultaneous depth analysis of σ for SiO_2+/CIGS and SiO_2-/CIGS we take only its final value as the common parameter to fit both data sets, as the value inside the first layer is different for the positive and negative samples. Thereafter, $\sigma(E)$ is fitted assuming a two regions description for $\sigma(x)$. As we have tried before with good results, we perform a second fit of $\sigma(x)$ to a three steps function. All the fits are in fig. 3.21. For the sample containing SiO_2- the two regions description is apparently a good fit to the experimental data due to the proximity of the initial and final values. However, for SiO_2+/CIGS an intermediate step enhances the $\sigma(E)$ fit, and the σ depth dependence should follow a similar model for the two CIGS samples. Therefore, the three regions description is chosen as the best fit for the experimental data of σ.

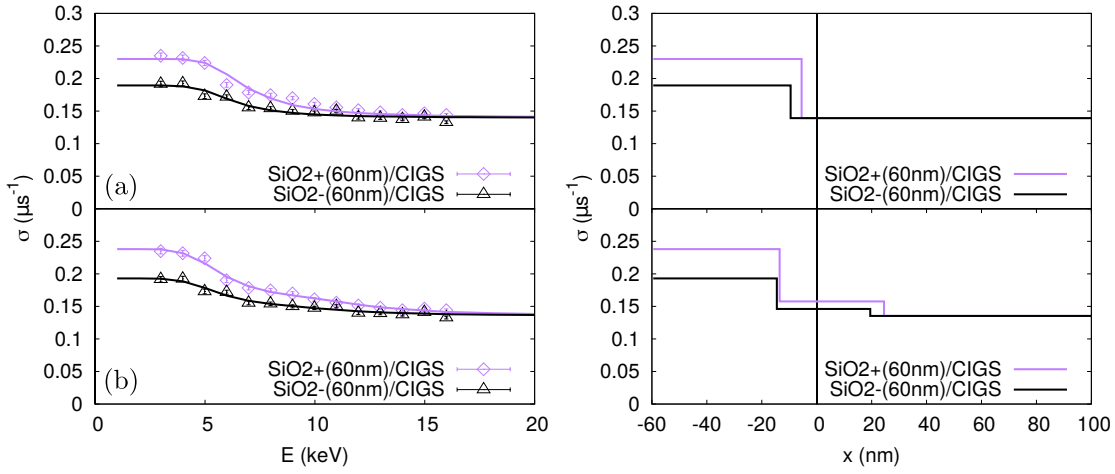

Figure 3.21: Left: The curves represent the predicted behavior of $\sigma(E)$ assuming a corresponding depth dependence as shown on the graph on the right for SiO_2+/CIGS (purple) and SiO_2-/CIGS (black). **Right:** Simultaneous fit of $\sigma(x)$ assuming a fit to a three step function for $SiO_2(+/-)$/CIGS samples, in which the final step value is equal.

Performing a visual evaluation of the fits obtained using simultaneous fitting methods, we conclude that the best descriptions of experimental data for both μSR parameters are acquired when fitting assuming common parameters in data sets from different samples, since they have a similar layer where the μSR parameter is expected to be the same.

Based on this observation, we will proceed to the analysis of the samples of Si with SiO_2+ and SiO_2-, applying the simultaneous fit analysis.

3.3.2.2 SiO_2+/Si and SiO_2-/Si

Starting with diamagnetic fraction measured for these samples, three different fits were performed, and are represented in fig. 3.22. As usual, the first fit of $f_{dia}(E)$ assumes a description of $f_{dia}(x)$ with two regions, which we can see does requires another step. The fits using a three steps function for $f_{dia}(x)$ can be performed considering one or two common parameters. This was previously discussed for the CIGS samples, where we saw that f_{dia} does not only have the same final value for both samples but also has the same initial value independently of the first layer charge. Therefore, both cases are tested for the Si samples.

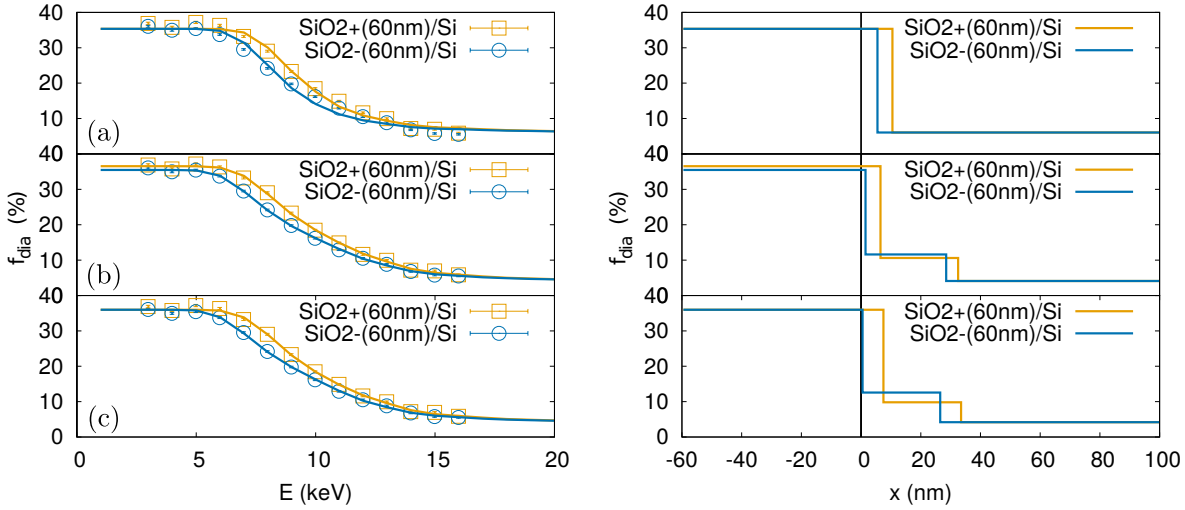

Figure 3.22: Left: The curves represent the predicted behavior of $f_{dia}(E)$ assuming a corresponding depth dependence as shown on the graph on the right for $SiO_2+/CIGS$ (purple) and $SiO_2-/CIGS$ (black). **Right: (a)** Simultaneous fit of $f_{dia}(x)$ assuming a fit to a three step function in which the final step value is equal for both samples. **(b)** Simultaneous fit of $f_{dia}(x)$ assuming a fit to a three step function in which the initial and final step values are equal for both samples.

Between the three steps fits illustrated in 3.22, we choose the last description, because having two common parameters simplifies the fit while still offering a good description of the experimental data.

The relaxation rate behavior follows what we observed in the CIGS samples, being that the value of σ inside the SiO_2 differs according to its charge.

The experimental data $\sigma(E)$ is fitted assuming a depth dependence described by two regions, as represented in fig. 3.23. This simultaneous fit provides a good description of the experimental data.

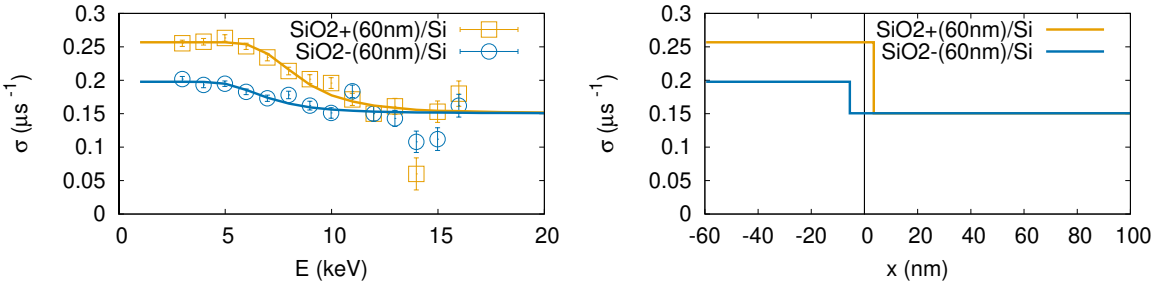

Figure 3.23: Left: The curves represent the predicted behavior of the parameter $\sigma(E)$ assuming a corresponding depth dependence as shown on the graph on the right for SiO_2+/Si (orange) and SiO_2-/Si (blue). **Right:** Simultaneous fit of $\sigma(x)$ assuming a fit to a two step function in which the final step value is equal for both samples.

3.4 Diamagnetic fraction

Considering all the depth resolved analysis performed in the previous sections, the fits depicted in fig. 3.20(b) and fig. 3.22(c) are here presented, as they offer the best representation of the experimental data.

The depth resolved analysis for the diamagnetic fraction for the $SiO_2(+/-)$/CIGS, CIGS and $SiO_2(+/-)$/Si samples is represented in fig. 3.24 and the fitting parameters obtained are gathered in table 3.3.

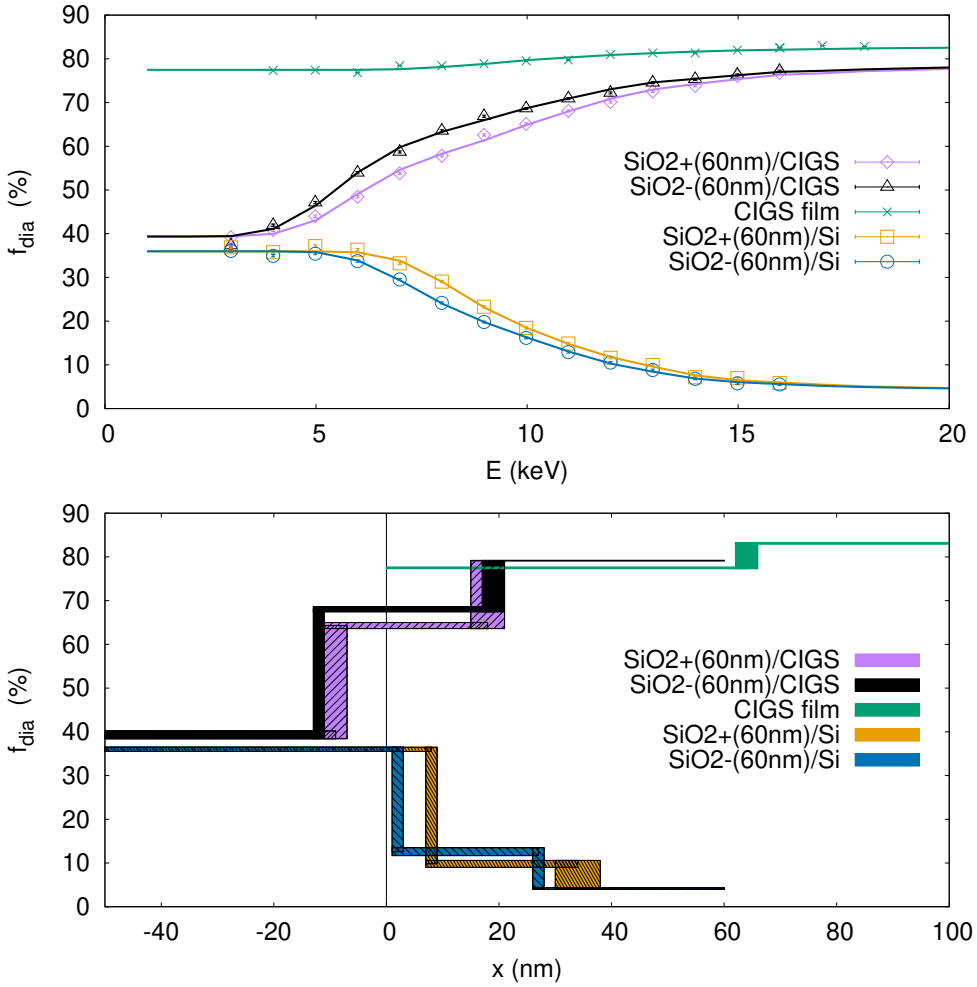

Figure 3.24: **(a)** Diamagnetic fraction as a function of muon implantation energy, $f_{dia}(E)$ for $SiO_2(+/-)$/CIGS, CIGS and $SiO_2(+/-)$/Si samples. The curves represent the predicted behavior of the parameter assuming a depth dependence as shown in the corresponding graph. **(b)** Simultaneous fit of $f_{dia}(x)$ assuming a fit to a three step function in which the initial and final step value is equal for the $SiO_2(+/-)$/CIGS and $SiO_2(+/-)$/Si samples. The CIGS sample is fitted assuming a fit to a two step function for $f_{dia}(x)$. The thickness of lines indicates the error associated with the fitting parameters of $f_{dia}(x)$.

	f_1 (%)	f_2 (%)	f_3 (%)	1st layer (nm)	2nd layer (nm)
CIGS (bulk)	77.5(2)	83.1(2)	–	64(2)	–
SiO_2+/CIGS	39.3(9)	64.3(9)	79.2(1)	51(2)	78(3)
SiO_2−/CIGS		69.0(6)		48(1)	79(2)
SiO_2+/Si	36.0(5)	9.8(9)	4.2(1)	68(1)	94(4)
SiO_2−/Si		12.6(9)		62(1)	87(1)

Table 3.3: Fitting parameters obtained in the depth-resolved analysis of the diamagnetic fraction, f_{dia}, for the fit approach depicted in fig. 3.24. The depth parameters are nominal values and give the position of the layer measured from the surface.

For CIGS film $f_{dia}(x)$ exhibits the existence of two regions. The dip in diamagnetic fraction at the CIGS surface measured using the μSR technique gives us the width of the surface defect layer, which is 64(2) nm (see table 3.3).

The experimental values used to obtain $f_{dia}(x)$ were measured for muon implantation energies between 3 and 16 keV. However, it is important to note that a maximum of implantation energy corresponds to very different average implantation depth in a single CIGS film, as compared to a sample within an additional 60nm dielectric layer on top of CIGS. The stopping probability distributions presented in fig. 3.10 show that inside SiO_2/CIGS samples we are probing a region from SiO_2 surface to about 120 nm. In other words, in SiO_2/CIGS samples we are probing only up to 60 nm within the CIGS layer, barely reaching the end of the surface defect layer measured in CIGS film. Hence explaining why we do not obtain the final f_{dia} value equal to the final f_{dia} value of CIGS, as expected.

Comparing the behavior of the μSR parameters in samples containing CIGS and Si, the most significant distinction is the depth at which the step transitions occurs. For example, looking at $f_{dia}(x)$ in CIGS samples coated with $Si_2(+/-)$, the first step transition occurs well inside the first layer. This observation contrasts with the $f_{dia}(x)$ behavior in samples containing Si as the bottom layer, in which the first transition occurs at SiO_2/Si interface inside the Si layer.
This distinct behavior could be due to difference in thickness of the SiO_2 layer between the samples containing CIGS and Si. However, this explanation is unlikely because, as mentioned previously, the CIGS and Si samples with the same fixed charge SiO_2, had their top layers deposited simultaneously.
On the other hand the observation points to the occurrence of intermixing between the dielectric and the CIGS layers, which alters the SiO_2 structure close to the interface, which could justify the intermediate f_{dia} step starting still inside SiO_2.

There is a noticeable difference in f_{dia} intermediate step value between samples with positive and negative charge density on the top layer. In fig. 3.24 we see this fraction is higher for both CIGS and Si samples containing SiO_2+. This is likely due to the different temperature conditions the SiO_2+ and SiO_2− are deposited. In [Cun+18], SiO_x - 300 °C is said to be

have more recombination channels present, when compared to a SiO_x deposited at T=150 °C. The diamagnetic fraction is known to be sensitive to the defect content so it is possible that the observed differences in SiO_2+ and SiO_2- samples are due to difference in defect content. However, a sensitivity of the muon probe to the sign of the charge cannot be ruled out. The μSR information needs to be complemented with information from other experimental techniques for a full interpretation of the data.

3.5 Relaxation rate

Considering all the depth resolved analysis performed in the previous sections, the fits depicted in fig. 3.21(b) and fig. 3.23 were chosen as the best analysis of the experimental data.

The relaxation rate of the same samples, the fits obtained are in fig. 3.25 and the respective parameters are shown in table 3.4.

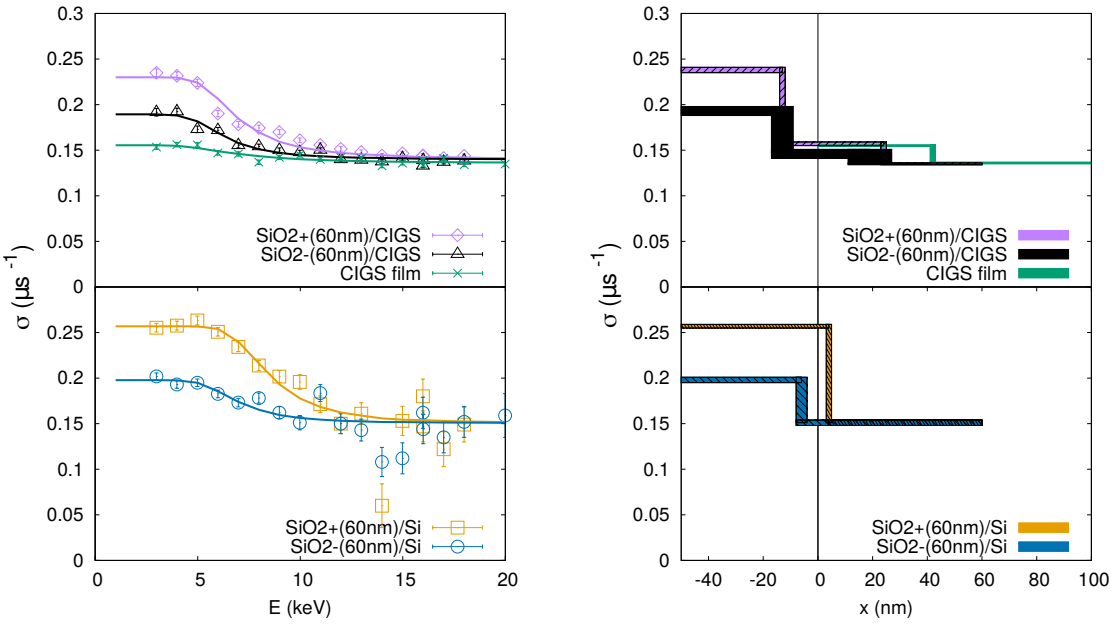

Figure 3.25: Left: Relaxation rate as a function of muon implantation energy, $\sigma(E)$ for $SiO_2(+/-)$/CIGS, CIGS (a) and $SiO_2(+/-)$/Si (b) samples. The curves represent the predicted behavior of the parameter assuming a depth dependence as shown in the corresponding graph. **Right: (a)** Simultaneous fit of $\sigma(x)$ assuming a fit to a three step function in which the final step value is equal for the $SiO_2(+/-)$/CIGS samples. The CIGS sample is fitted assuming a fit to a two step function for $\sigma(x)$. **(b)** Simultaneous fit of $\sigma(x)$ assuming a fit to a two step function in which the final step value is equal for the $SiO_2(+/-)$/Si samples The thickness of lines indicates the error associated with the fitting parameters of $\sigma(x)$.

Comparing the behavior in samples containing CIGS and Si, a difference in the depth at which the step transitions occurs is observed. This effect is similar to the one observed in the fractions, which was suggested to be due to an intermixing at the SiO_2/CIGS interface.

Comparing the relaxation rate for SiO_2+ and SiO_2-, the value for the first one is significantly larger. The increment in the relaxation rate for SiO_2+ suggests the presence of a paramagnetic component, which corresponds to the formation of muonium. This formation probability is possibly affected by the sample preparation parameters conditions, which were different for

	σ_1 (μs^{-1})	σ_2 (μs^{-1})	σ_3 (μs^{-1})	1st layer (nm)	2nd layer (nm)
CIGS (bulk)	0.155(1)	0.136(1)	–	42(1)	–
SiO_2+/CIGS	0.238(3)	0.157(2)	0.135(1)	47(1)	84(1)
SiO_2−/CIGS	0.193(5)	0.146(5)		47(4)	79(8)
SiO_2+/Si	0.257(2)	0.151(3)	–	64(1)	–
SiO_2−/Si	0.198(3)		–	54(2)	–

Table 3.4: Fitting parameters obtained in the depth-resolved analysis of the relaxation rate, σ, for the fit approach depicted in fig. 3.25. The depth parameters are nominal values and give the position of the layer measured from the surface.

the positive and negative SiO_2, being that SiO_2+ was processed at a higher temperature. This can also be due to a different defect concentration, as suggested before.

4

Conclusion and Future Perspectives

The work developed throughout this project had two main focuses:

- developing the existing tool for depth-resolved analysis of Muon Spin Spectroscopy (μSR) data in multi-layered systems;
- advancing the understanding of the effect that different fixed charges have on CIGS surface as well as to study the contribution of a SiO_2 dielectric layer on the passivation of SiO_2/CIGS interface using μSR.

4.1 Depth-resolved analysis tool for simultaneous fits

A MATLAB depth-resolved analysis tool for muon spin spectroscopy named DREAM was developed by Simões et al. DREAM fits μSR data measured as function of muon implantation depth, by establishing a relation between implantation energy and the average stopping depth of the muon. Therefore, it uses the experimental energy dependent results and the stopping probability per unit length $P(x,E)$ to obtain a description of the behavior of a given μSR parameter as function of muon implantation depth. For the context of this work, DREAM features were enhanced in order to perform simultaneous fits, and to allow for a simpler use of this tool.

From the user point of view, the processes of loading and saving the fit data was made simpler, without having to alter the MATLAB code between runs. This contributes to reducing the set-up times necessary to use DREAM and making this tool more accessible.

The simultaneous fit feature can fit two data sets at the same time, when the fit parameters are expected to be common. Two types of simultaneous fits were developed, which use different common fit parameters according to the experimental data sets.

The simultaneous fit features of DREAM were tested and used on the analysis performed for the μSR data.

Simultaneous fit within the same sample

Two μSR sets of data measured for the same sample can be fitted at the same time, as we assume their depth dependence has a similar behavior, and the transition between regions happens at the same depth within the sample. This was the case for the diamagnetic fraction and spin relaxation of a SiO_2+/CIGS, represented in fig. 4.1. The diamagnetic fraction and the relaxation were simultaneously fitted, assuming the intermediate step of the depth dependent description occurs within the same region for both μSR data sets and provides a good fit to the experimental data.

We have demonstrated that two data sets measured for a given sample can be simultaneously fitted when both μSR parameters are sensitive to variations of composition within the sample.

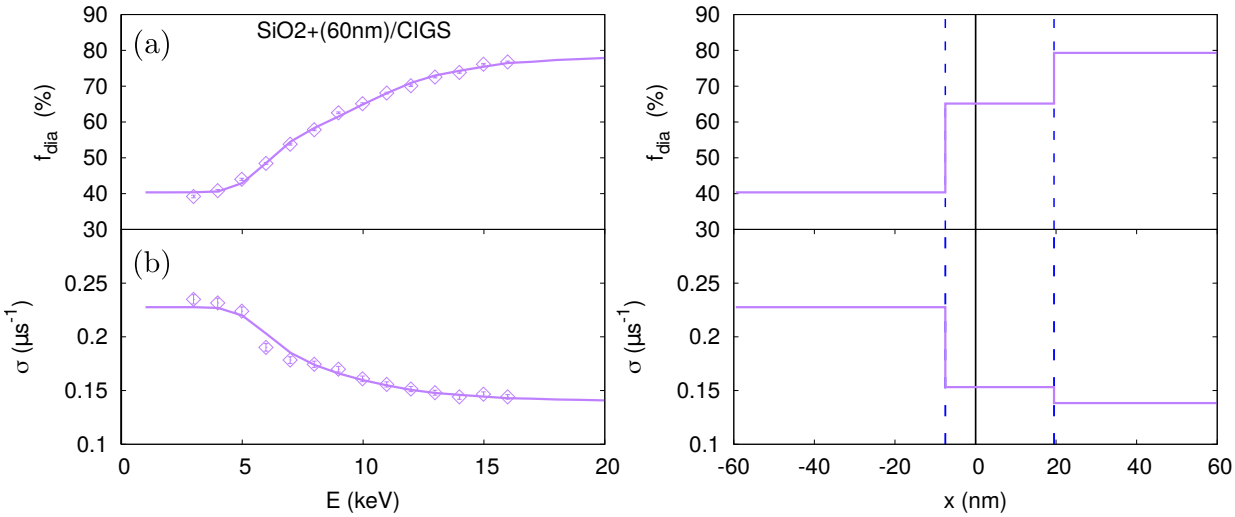

Figure 4.1: Left: The curve represents the predicted behavior of **(a)** $f_{dia}(E)$ and **(b)** $\sigma(E)$ assuming a corresponding depth dependence as shown on the graph on the right for SiO_2+/CIGS. **Right:** Simultaneous fit of **(a)** $f_{dia}(x)$ and **(b)** $\sigma(x)$ assuming a three steps description with an intermediate region occurring at the same depth. The black vertical line is placed at the interface position, and the blue dashed lines show the common transitions between steps for $f_{dia}(x)$ and $\sigma(x)$.

Simultaneous fit of different samples

The second simultaneous fit can be performed for two data sets measured for a given μSR parameter for two different samples which have at least a layer with the same composition. Taking the analysis performed for SiO_2+/CIGS and SiO_2−/CIGS (fig. 4.2), the values of diamagnetic fraction are equal within the SiO_2 and CIGS layers. This information is used when fitting $f_{dia}(x)$ for the two samples, and the initial and final are considered common fit parameters.

The simultaneous fit of different sample proves useful and provides a good description of the two data sets when the samples have ate least a layer where the μSR parameter has the same value.

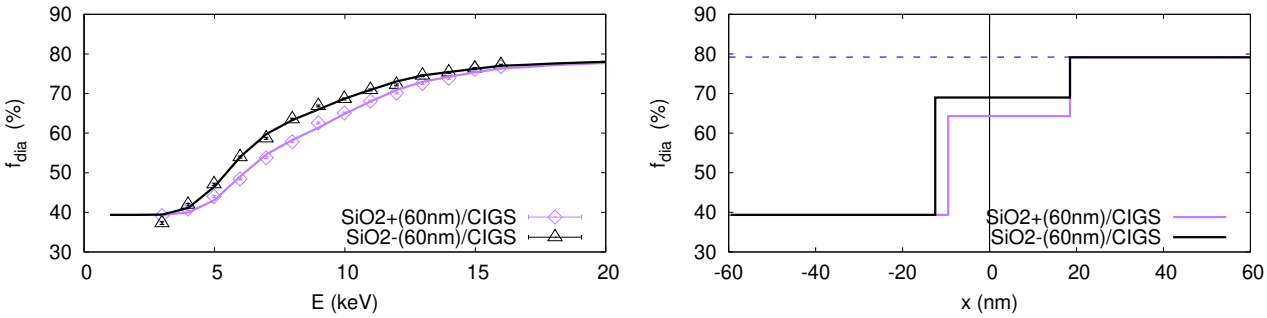

Figure 4.2: Left: The curves represent the predicted behavior of $f_{dia}(E)$ assuming a corresponding depth dependence as shown on the graph on the right for SiO_2+/CIGS and SiO_2−/CIGS. **Right:** Simultaneous fit of $f_{dia}(x)$ for SiO_2+/CIGS and SiO_2−/CIGS assuming a three steps description where the first and final steps have equal f_{dia}. The black vertical line is placed at the interface position, and the blue dashed line shows the final step where f_{dia} is common.

4.2 SiO_2/CIGS

SiO_2/CIGS and CIGS

In SiO_2/CIGS the final value of the diamagnetic fraction was expected to be equal to the CIGS value in bulk. The results for CIGS film (fig. 3.24) show a surface defect layer with a width equal to 64(2) nm, and the placement of SiO_2 does not seem to contribute to the reduction of the width of this region. Muon implantation energy measurements between 3 and 16 keV in samples with a SiO_2 layer are able to probe the sample from surface to about 60 nm within CIGS, and up to around 60 nm no reduction of the surface defect layer was observed (fig. 3.24).

SiO_2/CIGS vs SiO_2/Si

The bilayer systems SiO_2/CIGS require a three step description of the diamagnetic fraction as function of muon implantation depth, and this is also the case for SiO_2/Si samples (fig. 3.24). However, the intermediate step occurs for different regions within the SiO_2/CIGS and SiO_2/Si samples. The $f_{dia}(x)$ intermediate step, in fig. 3.24, starts within the first layer of SiO_2 for the SiO_2/CIGS samples, whereas for Si samples, the intermediate region starts close to the interface inside the Si layer. This observation could be an indication of a difference in the thickness of the SiO_2 layer between the CIGS and Si samples. However, this case is unlikely because the samples with equal charges had the SiO_2 simultaneously deposited. Hence, the observation can be explained with the occurrence of intermixing due the formation of SiO_2/CIGS interface, which is detected due to the sensitivity of the signal to changes in the muon environment.

The results of relaxation rate as function of implantation depth, in fig. 3.25, also show a distinctive transition behavior between samples with Si and CIGS, as observed for the diamagnetic fraction, which was suggested to be due to an intermixing at the SiO_2/CIGS interface.

SiO_2+ vs SiO_2-

As for the effect of different charges, in both Si and CIGS interfaces with SiO_2+ (fig. 3.24), the intermediate region in the step-like description of diamagnetic fraction as function of muon implantation depth shows a lower fraction value for the positive sample. This agrees with the observation in [Cun+18], where the sample containing positive SiO_2, which was deposited at a higher temperature, shows evidences of having more recombination channels in the interface. In terms of μSR measurements, this translates in a larger missing fraction, which is consistent with the differences between the interface diamagnetic values for SiO_2+/CIGS and SiO_2-/CIGS. Therefore, the different deposition conditions of SiO_2 with positive and negative fixed charges can contribute to this observation, although the sensitivity of the muon probe to the sign of the charge is also to be considered.

The muon spin relaxation dependence with implantation depth, in fig. 3.25, has a significantly larger value within the first region in SiO_2 with a positive charge density, when compared to the sample containing SiO_2 with negative fixed charges. This suggests the presence of a paramagnetic component due to muonium formation, which can also be attributed to a different defect concentration.

4.3 Future perspectives

This work contributes to the study of the effect that opposite polarity insulator layers have on the interface formed with CIGS. The results presented in this work clearly reinforce muon spin spectroscopy as a privileged technique for the microscopic investigation of nanostructures. However, this use of the technique is still in infancy and requires a strong support by other techniques for a solid interpretation. The results obtained can be complemented with other techniques, such as transmission electron microscopy (TEM), which can provide measurements of the width of the first dielectric layer. This complementary information should be used in order to perform a more throughout interpretation and revision of the μSR results.

The tool for depth-resolved analysis for muons (DREAM) has also been improved during this work in order to provide a better interpretation of the data collected for the samples studied. However, the analysis can be used and extended to the μSR study of other semiconductor systems. Furthermore, DREAM has become more user-friendly and its use as an analysis tool does not require any code manipulation skills. However, as future work, some aspects related to the introduction of information can be revised and simplified.

Bibliography

[Alb+18] H. V. Alberto et al. "Slow-muon study of quaternary solar-cell materials: Single layers and *p-n* junctions". In: *Physical Review Materials 2* (Feb. 2018).

[All10] Giuseppe Allodi. *FMINUIT - A binding to Minuit for Matlab, Octave Scilab. Version 2.3.1.* May 2010. URL: https://www.fis.unipr.it/~giuseppe.allodi/Fminuit/Fminuit_intro.html.

[Ama19] Alex Amato. *Physics with Muons: From Atomic Physiscs to Solid State Physics*. Mar. 2019. URL: https://www.psi.ch/en/lmu.

[Blu99] S. J. Blundell. "Spin-polarized muons in condensed matter physics". In: *Contemporary Physics* (1999).

[BM04] Pavel Bakule and Elvezio Morenzoni. "Generation and application of slow polarized muons". In: *Contemporary Physics* (2004).

[Bos+19] S. Bose et al. "A morphological and electronic study of ultrathin rear passivated Cu(In,Ga)Se2 solar cells". In: *Thin Solid Films* 671 (2019), pp. 77–84. ISSN: 0040-6090. DOI: https://doi.org/10.1016/j.tsf.2018.12.028.

[Bre+73] J. H. Brewer et al. "Anomalous μ^+ Precession in Silicon". In: *Phys. Rev. Lett.* 31 (3 July 1973), pp. 143–146.

[Bro11] Gregory Ferguson Brown. "The Effects of Non-Uniform Electronic Properties on Thin Film Photovoltaics". PhD thesis. UC Berkeley., 2011. URL: https://escholarship.org/uc/item/30t6135k.

[CS86] S.F.J. Cox and M.C.R. Symons. "Molecular radical models for the muonium centres in solids". In: *Chemical Physics Letters* 126.6 (1986), pp. 516–525. ISSN: 0009-2614.

[Cun+18] J. M. V. Cunha et al. "Insulator Materials for Interface Passivation of Cu(In,Ga)Se2 Thin Films". In: *IEEE Journal of Photovoltaics* 8.5 (2018), pp. 1313–1319.

[Dul+01] T Dullweber et al. “A new approach to high-efficiency solar cells by band gap grading in Cu(In,Ga)Se2 chalcopyrite semiconductors”. In: *Solar Energy Materials and Solar Cells* 67.1 (2001). PVSEC 11 - PART III, pp. 145–150. ISSN: 0927-0248. DOI: https://doi.org/10.1016/S0927-0248(00)00274-9.

[FPS08] D.M. Fleetwood, S.T. Pantelides, and Ronald Schrimpf. *Defects in microelectronic materials and devices*. Jan. 2008, pp. 1–755.

[Fro19] Solar Frontier. *Solar Frontier Achieves World Record Thin-Film Solar Cell Efficiency of 23.35%*. Jan. 17, 2019. URL: http://www.solar-frontier.com/eng/news/2019/0117_press.html (visited on 04/15/2020).

[Gre+19] Martin A. Green et al. “Solar cell efficiency tables (Version 53)”. In: *Progress in Photovoltaics: Research and Applications* 27.1 (2019), pp. 3–12. DOI: 10.1002/pip.3102.

[Gro] LEM: Low-Energy Muons Group. *Low Energy Muons: Overview of the Experimental Setup*. URL: https://www.psi.ch/en/low-energy-muons/experimental-setup (visited on 06/30/2020).

[ISE15] Fraunhofer ISE. *Current and Future Cost of Photovoltaics. Long-term Scenarios for Market Development, System Prices and LCOE of Utility-Scale PV Systems.Study on behalf of Agora Energiewende.* 2015. URL: https://www.ise.fraunhofer.de/content/dam/ise/de/documents/publications/studies/AgoraEnergiewende_Current_and_Future_Cost_of_PV_Feb2015_web.pdf (visited on 06/30/2020).

[ISE20] Fraunhofer ISE. *Photovoltaics Report*. June 23, 2020. URL: https://www.ise.fraunhofer.de/content/dam/ise/de/documents/publications/studies/Photovoltaics-Report.pdf (visited on 06/30/2020).

[JW04] Fred James and Matthias Winkler. *Minuit user’s guide*. 2004.

[KAB17] S.M. Karazi, I.U. Ahad, and K.Y. Benyounis. “Laser Micromachining for Transparent Materials”. In: *Reference Module in Materials Science and Materials Engineering*. Elsevier, 2017. ISBN: 978-0-12-803581-8. DOI: https://doi.org/10.1016/B978-0-12-803581-8.04149-7. URL: http://www.sciencedirect.com/science/article/pii/B9780128035818041497.

[Kie+88] R. F. Kiefl et al. “^{29}Si Hyperfine Structure of Anomalous Muonium in Silicon: Proof of the Bond-Centered Model”. In: *Phys. Rev. Lett.* 60 (3 Jan. 1988), pp. 224–226.

[Kua+89] Y. Kuang et al. “Formation of the negative muonium ion and charge-exchange processes for positive muons passing through thin metal foils”. In: *Phys. Rev. A* 39 (12 June 1989), pp. 6109–6123. DOI: 10.1103/PhysRevA.

39.6109. URL: https://link.aps.org/doi/10.1103/PhysRevA.39.6109.

[LE17] Taesoo D. Lee and Abasifreke U. Ebong. "A review of thin film solar cell technologies and challenges". In: *Renewable and Sustainable Energy Reviews* 70 (2017), pp. 1286–1297. ISSN: 1364-0321.

[Li+18] Jian V. Li et al. "Electrical properties of CdS/Cu(In,Ga)Se2 interface". In: *Japanese Journal of Applied Physics* 57.8 (June 2018), p. 085701. DOI: 10.7567/jjap.57.085701.

[Liu+99] W. Liu et al. "High Precision Measurements of the Ground State Hyperfine Structure Interval of Muonium and of the Muon Magnetic Moment". In: *Phys. Rev. Lett.* 82 (4 Jan. 1999), pp. 711–714.

[ME09] Ulf Malm and Marika Edoff. "Simulating material inhomogeneities and defects in CIGS thin-film solar cells". In: *Progress in Photovoltaics: Research and Applications* 17.5 (2009), pp. 306–314. DOI: 10.1002/pip.888. eprint: https://onlinelibrary.wiley.com/doi/pdf/10.1002/pip.888.

[Mol16] Fabien Mollica. "Optimization of ultra-thin Cu(In,Ga)Se2 based solar cells with alternative back-contacts". Theses. Université Pierre et Marie Curie - Paris VI, Dec. 2016. URL: https://tel.archives-ouvertes.fr/tel-01545671.

[Mor+02] E. Morenzoni et al. "Implantation studies of keV positive muons in thin metallic layers". In: *Nuclear Instruments and Methods in Physics Research Section B: Beam Interactions with Materials and Atoms* 192.3 (2002), pp. 254–266. ISSN: 0168-583X. DOI: https://doi.org/10.1016/S0168-583X(01)01166-1.

[Nak+19] Motoshi Nakamura et al. "Cd-Free Cu(In,Ga)(Se,S)2 Thin-Film Solar Cell With Record Efficiency of 23.35%". In: *IEEE Journal of Photovoltaics* 9 (Sept. 2019), pp. 1863–1867. DOI: 10.1109/JPHOTOV.2019.2937218.

[NRE] National Renewable Energy Laboratory NREL. *Best Research-Cell Efficiency Chart*. URL: https://www.nrel.gov/pv/cell-efficiency.html (visited on 03/26/2020).

[Pat88] Bruce D. Patterson. "Muonium states in semiconductors". In: *Rev. Mod. Phys.* 60 (1 Jan. 1988), pp. 69–159. DOI: 10.1103/RevModPhys.60.69.

[Pow+17] Michael Powalla et al. "Advances in Cost-Efficient Thin-Film Photovoltaics Based on Cu(In,Ga)Se2". In: *Engineering* 3.4 (2017), pp. 445–451. ISSN: 2095-8099. DOI: https://doi.org/10.1016/J.ENG.2017.04.015.

[Pro+07] T. Prokscha et al. “Formation of Hydrogen Impurity States in Silicon and Insulators at Low Implantation Energies”. In: *Phys. Rev. Lett.* 98 (22 May 2007), p. 227401. DOI: 10.1103/PhysRevLett.98.227401.

[REN19] REN21. *Renewable 2019 Global Status Report*. Paris: REN21 Secretariat, 2019, pp. 41–42, 94–95. URL: https://www.ren21.net/gsr-2019/.

[Rib+20] Ribeiro, Eduardo et al. “CdS versus ZnSnO buffer layers for a CIGS solar cell: a depth-resolved analysis using the muon probe”. In: *EPJ Web Conf.* 233 (2020), p. 05004. DOI: 10.1051/epjconf/202023305004.

[RS17] Jeyakumar Ramanujam and Udai P. Singh. “Copper indium gallium selenide based solar cells – a review”. In: *Energy Environ. Sci* 10 (6 Oct. 2017), pp. 1306–1319.

[Rud+05] D. Rudmann et al. “Sodium incorporation strategies for CIGS growth at different temperatures”. In: *Thin Solid Films* 480-481 (2005). EMRS 2004, pp. 55–60. ISSN: 0040-6090. DOI: https://doi.org/10.1016/j.tsf.2004.11.071.

[Sal11] Pedro Manuel Parracho Salomé. “ Chalcogenide thin films for solar cells: growth and properties”. PhD thesis. Universidade de Aveiro, Jan. 2011. URL: http://hdl.handle.net/10773/3723.

[Sie17a] Susanne Siebentritt. “Chalcopyrite compound semiconductors for thin film solar cells”. In: *Current Opinion in Green and Sustainable Chemistry* 4 (2017). 4 Novel materials for energy production and storage 2017, pp. 1–7. ISSN: 2452-2236. DOI: https://doi.org/10.1016/j.cogsc.2017.02.001.

[Sie17b] Susanne Siebentritt. “Chalcopyrite compound semiconductors for thin film solar cells”. In: *Current Opinion in Green and Sustainable Chemistry* 4 (2017). 4 Novel materials for energy production and storage 2017, pp. 1–7. ISSN: 2452-2236. DOI: https://doi.org/10.1016/j.cogsc.2017.02.001. URL: http://www.sciencedirect.com/science/article/pii/S2452223616300670.

[Sim+20] A. Simões et al. “Muon implantation experiments in films: Obtaining depth-resolved information”. In: *Review of Scientific Instruments* 91 (Feb. 2020), p. 023906. DOI: 10.1063/1.5126529.

[Sim19] André Filipe Almeida Simões. “Depth Resolved Information in Muon Implantation Experiments in Films”. Master. Universidade de Coimbra, July 2019.

[Sme+16] Arno HM Smets et al. *Solar energy. The physics and engineering of photovoltaic conversion, technologies and systems*. UIT Cambridge, England, 2016.

[Son19] Stuttgart: Zentrum für Sonnenenergie und Wasserstoff-Forschung Baden-Württemberg. *CIGS White Paper 2019*. 2019. URL: https://cigs-pv.net/wortpresse/wp-content/uploads/2019/04/CIGS_White_Paper_2019_online.pdf (visited on 06/30/2020).

[SS11] Roland Scheer and Hans-Werner Schock. "Thin Film Technology". In: *Chalcogenide Photovoltaics*. 2011. Chap. 5, pp. 235–275. ISBN: 9783527633708. DOI: 10.1002/9783527633708.ch5.

[SW12] A. Suter and B.M. Wojek. "Musrfit: A Free Platform-Independent Framework for μSR Data Analysis". In: *Physics Procedia* 30 (2012), pp. 69–73. ISSN: 1875-3892. DOI: 10.1016/j.phpro.2012.04.042. URL: http://dx.doi.org/10.1016/j.phpro.2012.04.042.

[Ver+12] Bart Vermang et al. "Approach for Al2O3 rear surface passivation of industrial p-type Si PERC above 19%". In: *Progress in Photovoltaics: Research and Applications* 20.3 (2012), pp. 269–273. DOI: 10.1002/pip.2196.

[Vil+03a] R.C. Vilão et al. "Hydrogen states in CuInSe2—a μSR study". In: *Physica B: Condensed Matter* 340-342 (2003). Proceedings of the 22nd International Conference on Defects in Semiconductors, pp. 965–968. ISSN: 0921-4526. DOI: https://doi.org/10.1016/j.physb.2003.09.199.

[Vil+03b] R.C. Vilão et al. "Muon diffusion and trapping in chalcopyrite semiconductors". In: *Physica B: Condensed Matter* 326.1 (2003), pp. 181–184. ISSN: 0921-4526. DOI: https://doi.org/10.1016/S0921-4526(02)01598-3.

[Vil07] Rui César Vilão. "Isolated hydrogen in II–VI zinc–chalcogenide widegap semiconductors modelled by the muon analogue". PhD. Universidade de Coimbra, 2007.

[Wad+01] T. Wada et al. "Characterization of the Cu(In,Ga)Se2/Mo interface in CIGS solar cells". In: *Thin Solid Films* 387.1 (2001). Proceeedings of Symposium N on Thin Film Photovoltaicmaterials of the E-MRS Spring Conference, pp. 118–122. ISSN: 0040-6090. DOI: https://doi.org/10.1016/S0040-6090(00)01846-0.

[WGW07] S.R. Wenham, M.A. Green, and M.E. Watt. *Applied Photovoltaics*. Earthscan, 2007. ISBN: 9781844074013.

Appendices

A

DREAM - Documentation

A.1 Depth REsolved Analysis for Muons

André Simões & Maria Martins
Version 1.2.0, 2020

Description

DREAM is a MATLAB fitting routine which uses the MINUIT based program Fminuit for optimization and chi-square minimization [JW04; All10]. Monte Carlo simulations TRIM.SP [Mor+02] are used to obtain the muon stopping probability per unit length for different implantation energies, required to calculate the depth dependence of μSR parameters measured as function of muon implantation energy. The μSR experimental data is fitted having depth values as free parameters. The program can fit one to two experimental data sets when both have the same muon implantation profile.

Getting started

Before running the fitting routine one needs to obtain the TRIM.SP data for all the samples studied. This data contains the distribution of muons stopping inside the sample at a certain depth, for various muon implantation energies.
As the previous version, the code used in DREAM is divided in two parts, but with some changes which improve its performance and make it more accessible for the user.

The first part consists of a script which calculates the muon stopping probability per unit length, based on the TRIM.SP results. The result will then be saved in a MATLAB variable, which contains all the necessary data to perform the μSR parameter fit.

The second routine will then take the experimental data and perform a fit of the μSR parameter as a function of implantation energy measured according to the model desired for the

parameter dependence with implantation depth. The program can be used to fit one to two sets of experimental data. Simultaneous fits can be performed when two data sets have depth or fit parameters in common and, most importantly, they have the same muon implantation stopping profile (simulated by TRIM.SP).

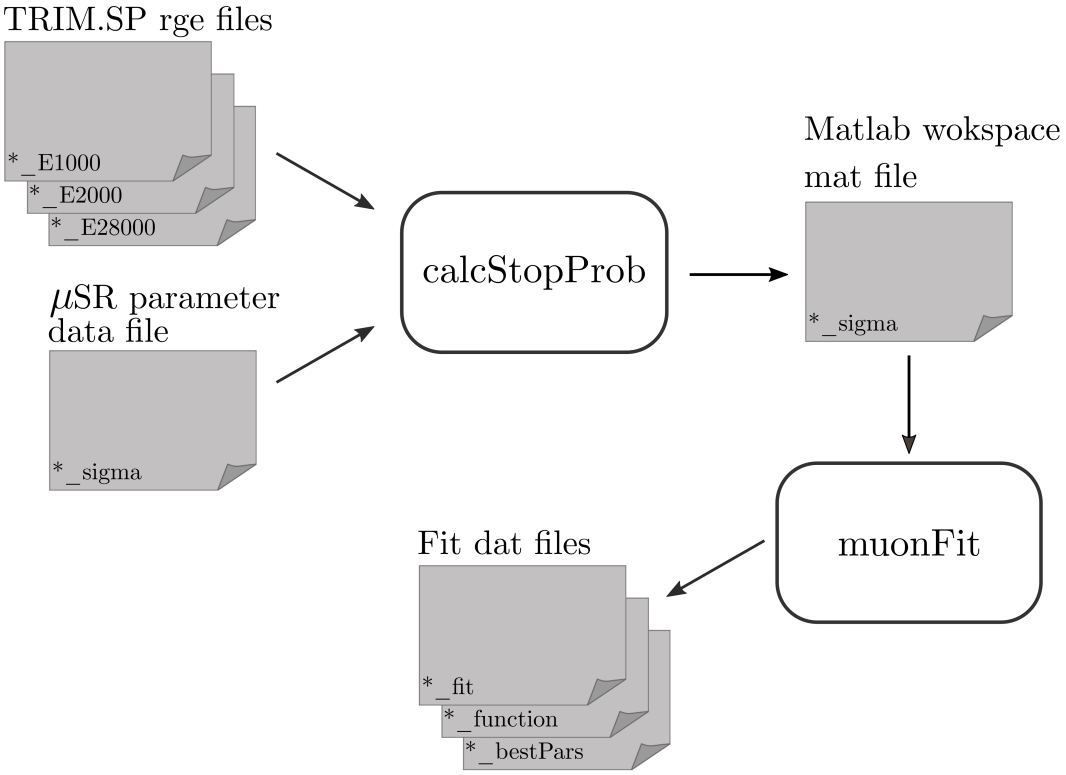

Figure A.1: General file flow to perform fits with DREAM.

Step-by-step instructions:

0. Perform TRIM.SP simulation for the sample under study (the muon implantation energy typically varies between 1 and 28 keV).

1. Place the files with extension *.rge* generated by TRIM.SP on the folder 'TRIMS.SP'.

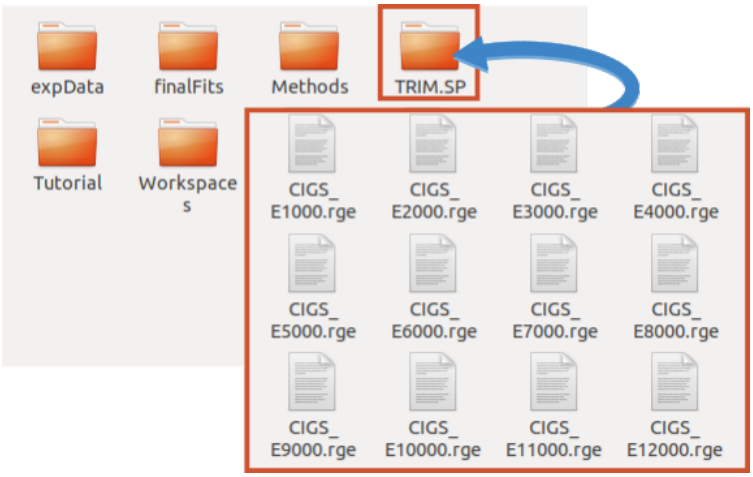

2. Create a *.dat* file for each μSR parameter f of a sample, and place the experimental data and its associated uncertainties in columns. The file should have three columns in the following order: E, f, δf, where E is the muon implantation energy, f is the measured values of the μSR parameter and δf its associated uncertainty.

3. Save the file as *sampleName_μSRparameter.dat* in the folder 'expData'. Take the example of a file with the relaxation data of a SiO_2+/CIGS sample, which is titled 'SiO_BR1_60nm_CIGS_sigma.dat'.

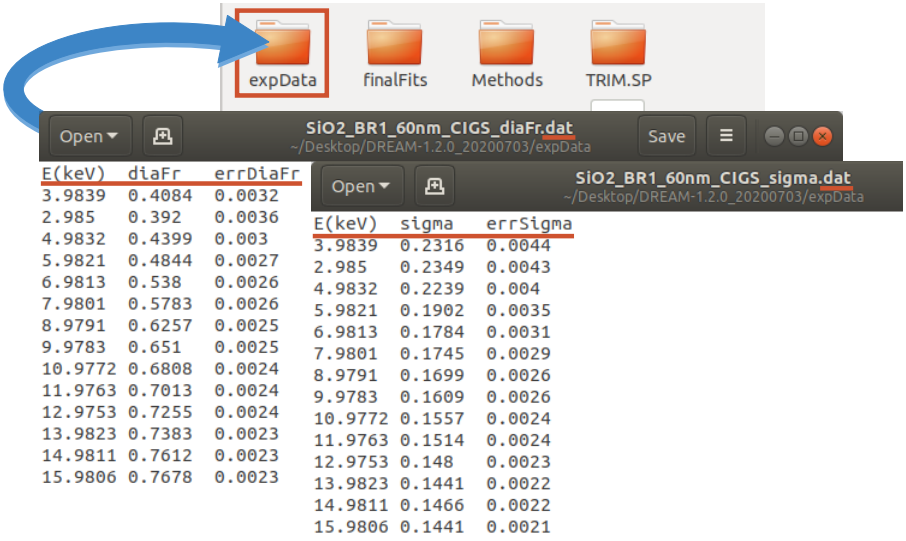

4. Open the program calcStopProb.m to calculate the muon stopping probability per unit length. In the 'EDITOR' separator click on 'RUN' or press F5. Running this program only requires the user provides the information requested. It results in the creation of a MATLAB workspace with the variables necessary to perform the fit, which will be stored in the folder 'Workspaces'. The MATLAB variable is titled after the input '*.dat' file but has the extension '.mat'. Repeat this step for all the experimental data sets you wish to fit.

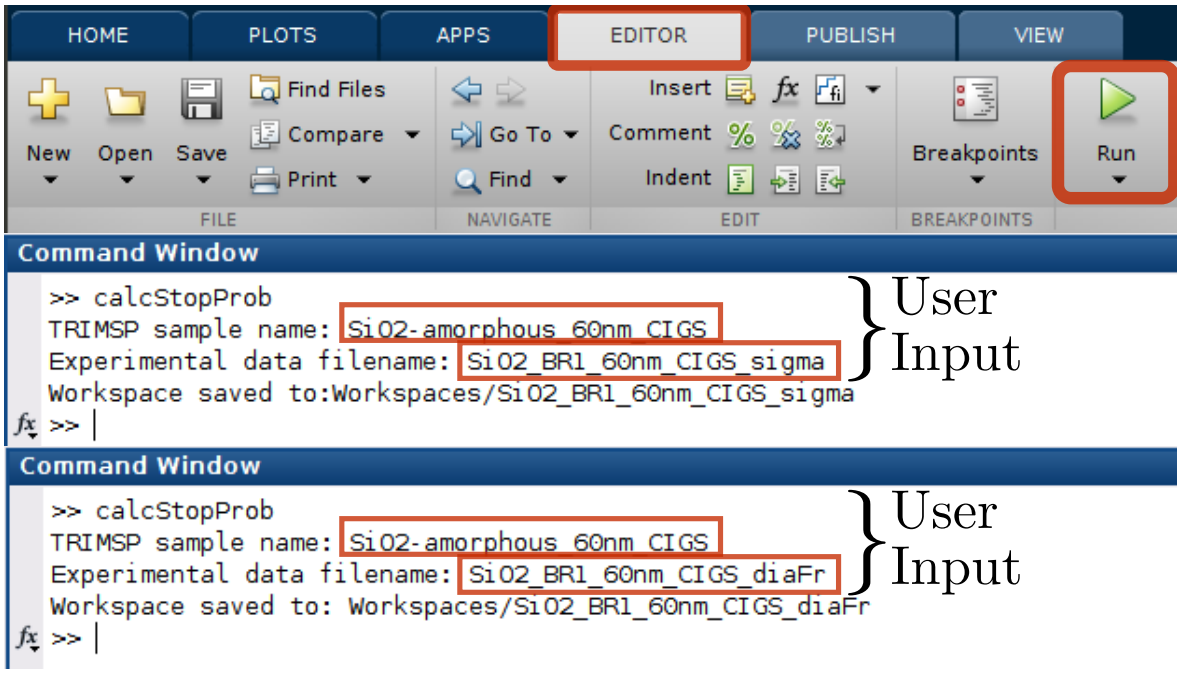

5. Go to the folder 'Methods' and open the program muonFit.m. As with the previous program the user needs only to provide the inputs requested in the MATLAB command window. The information required is:

   i. Type of fit to perform.

   ii. Data set to fit.

   iii. Initial values of the parameters and respective lower and upper bounds.

(a) Fit of a single data set:

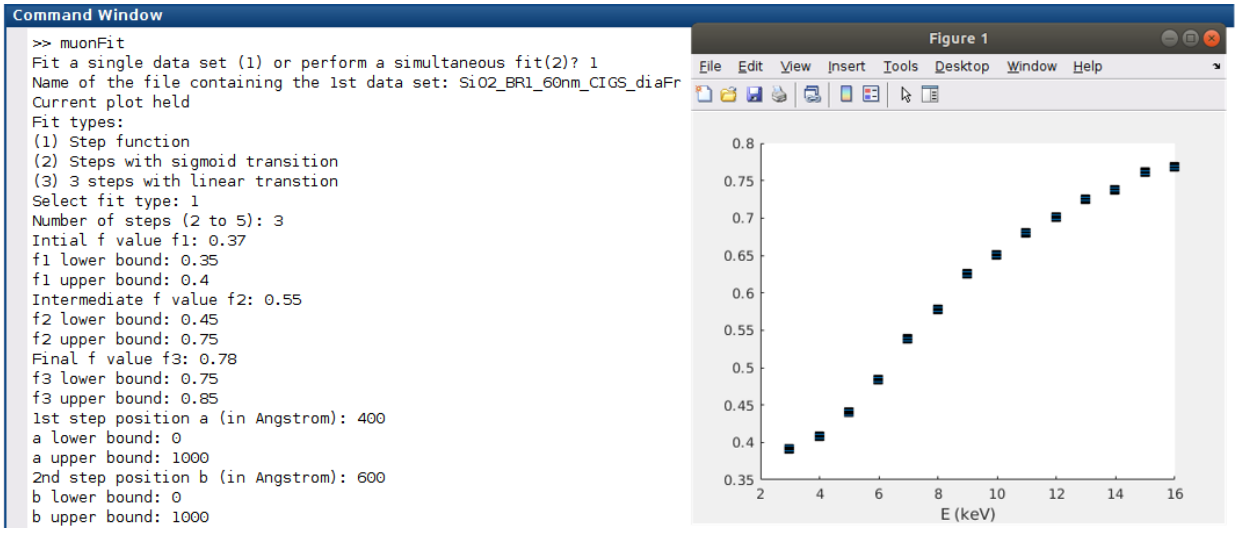

(b) Simultaneous fit of two data sets:

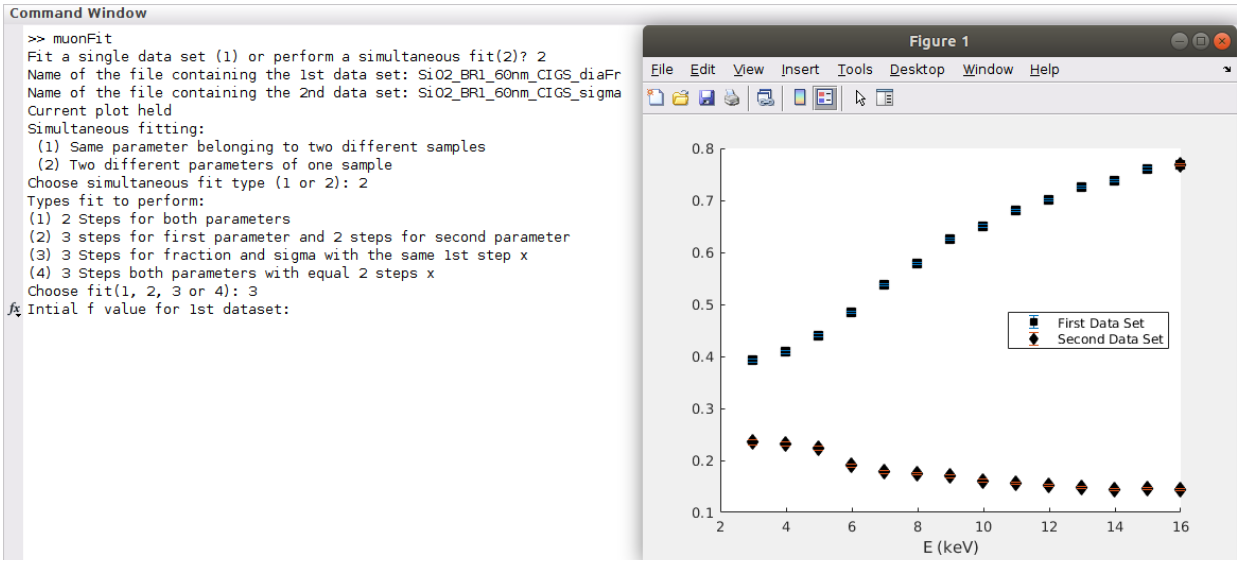

6. At this point we have all parameters required to start the minimization using the Fminuit function. Insert one of the following Minuit commands according to your goal:

   - **CALL 5**: displays the plot of the data introduced and respective fit.
   - **MIGRAD**: minimizes the function and calculates the fit parameters. Each call uses the previously calculated solution.
   - **MINOS**: calculates the associated errors to the fit parameters and its χ^2. This command should be called only after a good minimum has been found.
   - **EXIT**: exits Fminuit.

7. At the end of the routine the user can choose to save the fit parameters to the folder 'finalFits' and/or perform another fit to the same experimental data. Three files are created in 'finalFits' when the fitting result is saved:
   i. $*$**_fit.dat**: μSR parameter as function of muon implantation energy $f(E)$.
   ii. $*$**_function.dat**: μSR parameter as function of muon implantation depth $f(x)$.
   iii. $*$**_BestPars.dat**: best fit parameters and respective errors. This file also contains the value of reduced χ^2.

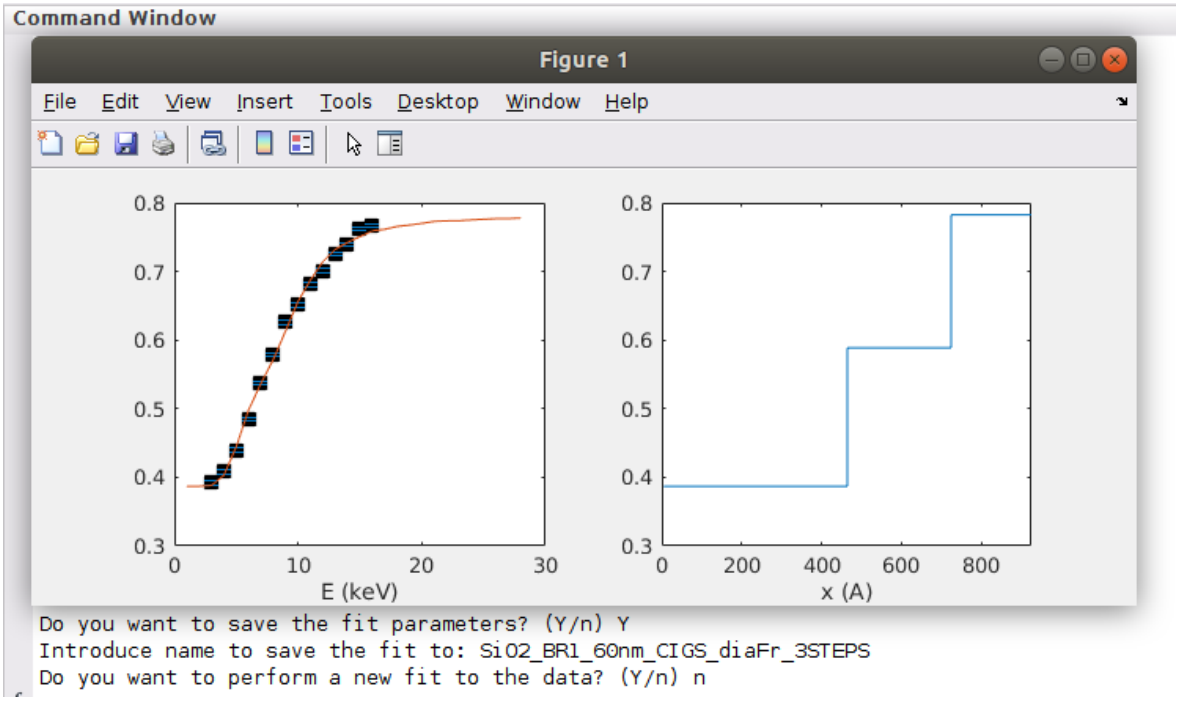

Code acknowledgments

[All10] Giuseppe Allodi. *FMINUIT - A binding to Minuit for Matlab, Octave Scilab. Version 2.3.1.* May 2010. URL: `https://www.fis.unipr.it/~giuseppe.allodi/Fminuit/Fminuit_intro.html`.

[Gar20] Damien Garcia. *Simpson's rule for numerical integration.* 2020. URL: `https://www.mathworks.com/matlabcentral/fileexchange/25754-simpson-s-rule-for-numerical-integration` (visited on 06/29/2020).

[Igo20] Igor. *WinOnTop version 1.6.0.0.* GitHub. 2020. URL: `https://github.com/i3v/WinOnTop` (visited on 06/29/2020).

[JW04] Fred James and Matthias Winkler. *Minuit user's guide.* 2004.

[Mor+02] E. Morenzoni et al. “Implantation studies of keV positive muons in thin metallic layers”. In: *Nuclear Instruments and Methods in Physics Research Section B: Beam Interactions with Materials and Atoms* 192.3 (2002), pp. 254–266. ISSN: 0168-583X. DOI: https://doi.org/10.1016/S0168-583X(01)01166-1.

[Sim+20] A. Simões et al. “Muon implantation experiments in films: Obtaining depth-resolved information”. In: *Review of Scientific Instruments* 91 (Feb. 2020), p. 023906. DOI: 10.1063/1.5126529.